

## ALCHEMI finds a “shocking” carbon footprint in the starburst galaxy NGC 253

NANASE HARADA,<sup>1,2</sup> SERGIO MARTÍN,<sup>3,4</sup> JEFFREY G. MANGUM,<sup>5</sup> KAZUSHI SAKAMOTO,<sup>6</sup> SEBASTIEN MULLER,<sup>7</sup>  
VÍCTOR M. RIVILLA,<sup>8</sup> CHRISTIAN HENKEL,<sup>9,10,11</sup> DAVID S. MEIER,<sup>12,13</sup> LAURA COLZI,<sup>8</sup> MITSUYOSHI YAMAGISHI,<sup>14</sup>  
KUNIIHIKO TANAKA,<sup>15</sup> KOUICHIRO NAKANISHI,<sup>1,2</sup> RUBÉN HERRERO-ILLANA,<sup>16,17</sup> YUKI YOSHIMURA,<sup>14</sup> P. K. HUMIRE,<sup>9</sup>  
REBECA ALADRO,<sup>9</sup> PAUL P. VAN DER WERF,<sup>18</sup> AND K. L. EMIG<sup>5,\*</sup>

<sup>1</sup>*National Astronomical Observatory of Japan, 2-21-1 Osawa, Mitaka, Tokyo 181-8588, Japan*

<sup>2</sup>*Department of Astronomy, School of Science, The Graduate University for Advanced Studies (SOKENDAI), 2-21-1 Osawa, Mitaka, Tokyo, 181-1855 Japan*

<sup>3</sup>*European Southern Observatory, Alonso de Córdova, 3107, Vitacura, Santiago 763-0355, Chile*

<sup>4</sup>*Joint ALMA Observatory, Alonso de Córdova, 3107, Vitacura, Santiago 763-0355, Chile*

<sup>5</sup>*National Radio Astronomy Observatory, 520 Edgemont Road, Charlottesville, VA 22903-2475, USA*

<sup>6</sup>*Institute of Astronomy and Astrophysics, Academia Sinica, 11F of AS/NTU Astronomy-Mathematics Building, No.1, Sec. 4, Roosevelt Rd, Taipei 10617, Taiwan*

<sup>7</sup>*Department of Space, Earth and Environment, Chalmers University of Technology, Onsala Space Observatory, SE-439 92 Onsala, Sweden*

<sup>8</sup>*Centro de Astrobiología (CSIC-INTA), Ctra. de Ajalvir Km. 4, Torrejón de Ardoz, 28850 Madrid, Spain*

<sup>9</sup>*Max-Planck-Institut für Radioastronomie, Auf dem Hügel 69, 53121 Bonn, Germany*

<sup>10</sup>*Astronomy Department, Faculty of Science, King Abdulaziz University, P. O. Box 80203, Jeddah 21589, Saudi Arabia*

<sup>11</sup>*Xinjinag Astronomical Observatory, Chinese Academy of Sciences, 830011 Urumqi, PR China*

<sup>12</sup>*New Mexico Institute of Mining and Technology, 801 Leroy Place, Socorro, NM 87801, USA*

<sup>13</sup>*National Radio Astronomy Observatory, PO Box O, 1003 Lopezville Road, Socorro, NM 87801, USA*

<sup>14</sup>*Institute of Astronomy, Graduate School of Science, The University of Tokyo, 2-21-1 Osawa, Mitaka, Tokyo 181-0015, Japan*

<sup>15</sup>*Department of Physics, Faculty of Science and Technology, Keio University, 3-14-1 Hiyoshi, Yokohama, Kanagawa 223-8522 Japan*

<sup>16</sup>*European Southern Observatory, Alonso de Córdova 3107, Vitacura, Casilla 19001, Santiago de Chile, Chile*

<sup>17</sup>*Institute of Space Sciences (ICE, CSIC), Campus UAB, Carrer de Magrans, E-08193 Barcelona, Spain*

<sup>18</sup>*Leiden Observatory, Leiden University, PO Box 9513, NL-2300 RA Leiden, The Netherlands*

### ABSTRACT

Centers of starburst galaxies may be characterized by a specific gas and ice chemistry due to their gas dynamics and the presence of various ice desorption mechanisms. This may result in a peculiar observable composition. We analyze abundances of CO<sub>2</sub>, a reliable tracer of ice chemistry, from data collected as part of the ALMA large program ALCHEMI, a wide-frequency spectral scan toward the starburst galaxy NGC 253 with an angular resolution of 1.6". We constrain the CO<sub>2</sub> abundances in the gas phase using its protonated form HOCO<sup>+</sup>. The distribution of HOCO<sup>+</sup> is similar to that of methanol, which suggests that HOCO<sup>+</sup> is indeed produced from the protonation of CO<sub>2</sub> sublimated from ice. The HOCO<sup>+</sup> fractional abundances are found to be  $(1 - 2) \times 10^{-9}$  at the outer part of the central molecular zone (CMZ), while they are lower ( $\sim 10^{-10}$ ) near the kinematic center. This peak fractional abundance at the outer CMZ is comparable to that in the Milky Way CMZ, and orders of magnitude higher than that in Galactic disk star-forming regions. From the range of HOCO<sup>+</sup>/CO<sub>2</sub> ratios suggested from chemical models, the gas-phase CO<sub>2</sub> fractional abundance is estimated to be  $(1 - 20) \times 10^{-7}$  at the outer CMZ, and orders of magnitude lower near the center. We estimate the CO<sub>2</sub> ice fractional abundances at the outer CMZ to be  $(2 - 5) \times 10^{-6}$  from the literature. A comparison between the ice and gas CO<sub>2</sub> abundances suggests an efficient sublimation mechanism. This sublimation is attributed to large-scale shocks at the orbital intersections of the bar and CMZ.

### 1. INTRODUCTION

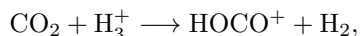
The abundance of interstellar molecules depends on the balance between their formation and destruction processes in the gas phase and on grain surfaces. Exchange processes can transform molecules in one phase to the other; gas-phase molecules can freeze onto dust

\* Jansky Fellow of the National Radio Astronomy Observatory

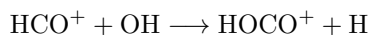
grains as ice (adsorption), while molecules on grain surfaces can sublime into the gas phase (desorption). Knowing both gas- and ice-phase abundances is, therefore, necessary for a comprehensive understanding of the chemical composition and their related physical conditions. Carbon dioxide ( $\text{CO}_2$ ) is one of the most dominant forms of ice on interstellar dust (Öberg et al. 2011) together with  $\text{H}_2\text{O}$  and  $\text{CO}$ .  $\text{CO}_2$  is, in fact, one of the ice species detectable in extragalactic sources (e.g., Lahuie et al. 2007; Yamagishi et al. 2015). It is obvious from the strong  $\text{CO}$  rotational emission that the gas-phase  $\text{CO}$  is abundant, but  $\text{CO}_2$  is thought to reside more preferentially on dust due to the inefficient gas-phase formation (Garrod & Pauly 2011). Because  $\text{CO}_2$  has higher desorption energy than that of  $\text{CO}$ , the presence of abundant gas-phase  $\text{CO}_2$  requires stronger desorption mechanisms. While  $\text{CO}_2$  can be detected via rotational-vibrational transitions in warm gas ( $\gtrsim$  several 100 K) (e.g., Boonman et al. 2003) or in ice with broader line features (e.g., Yamagishi et al. 2015), it cannot be observed in cold gas due to the lack of a permanent dipole moment.

Although the gas-phase abundances of such species without a dipole moment cannot be directly measured through commonly observed rotational transitions, it has been proposed that they can be estimated from their protonated forms (Herbst et al. 1977; Agúndez et al. 2015; Rivilla et al. 2019). The protonated form of  $\text{CO}_2$ ,  $\text{HOCO}^+$ , was first detected in Sgr B2 by Thaddeus et al. (1981), but its line identification required spectroscopic confirmation by Defreese et al. (1982). Since then,  $\text{HOCO}^+$  has been detected in translucent clouds (Turner et al. 1999), low-/high-mass star-forming regions (Sakai et al. 2008; Vastel et al. 2016; Majumdar et al. 2018; Fontani et al. 2018), the Galactic Center (Sgr A and B2 clouds; Minh et al. 1988, 1991), starburst galaxies (Martín et al. 2006; Aladro et al. 2015) and a  $z \sim 0.9$  molecular absorber (Muller et al. 2013). Among them, Minh et al. (1991) and Armijos-Abendaño et al. (2015) found about 2 orders of magnitude higher fractional abundances of  $\text{HOCO}^+$  in the Galactic Center than in spiral-arm molecular clouds.

The main formation paths of  $\text{HOCO}^+$  are gas-phase reactions: protonation of  $\text{CO}_2$  such as



or an ion-neutral reaction



(Vastel et al. 2016; Bizzocchi et al. 2017). In the former route, the  $\text{HOCO}^+$  abundance can increase due to the evaporation of  $\text{CO}_2$  from grain surfaces because  $\text{CO}_2$

is one of the most abundant forms of carbon on grain surfaces. The ice can sublime thermally (e.g., in the vicinity of protostars), or non-thermally (e.g., photodesorption, cosmic-ray-induced evaporation, or shock sputtering). While the latter route from  $\text{HCO}^+$  is considered dominant in at least some parts of high- or low-mass star-forming regions (Majumdar et al. 2018; Fontani et al. 2018), the protonation of  $\text{CO}_2$  can be the dominant route when there is a fast mechanism of  $\text{CO}_2$  sublimation.

Shocks, one of drivers of the ice sublimation process, are ubiquitous in galactic centers. In many barred-spiral galaxies, galactic centers host intersections of  $x_1$  and  $x_2$  orbits<sup>1</sup> (Athanasoula 1992; Seo & Kim 2013; Sormani & Li 2020). At these orbital intersections, shocks are naturally expected. Abundances of typical shock molecular tracers such as  $\text{CH}_3\text{OH}$  and  $\text{SiO}$  have been found to be enhanced at locations of orbital intersections in IC342 and M83 (Meier & Turner 2005; Harada et al. 2019).

In this paper, we report an enhancement of  $\text{HOCO}^+$  at the orbital intersections near the center of the starburst galaxy NGC 253. NGC 253 is one of the nearest ( $d = 3.5$  Mpc; Rekola et al. 2005) and most studied starburst galaxies. Its nuclear ring forms a central molecular zone (CMZ) within a few hundred parsec scale, with a mass of  $\sim 2 \times 10^8 M_\odot$  within a radius of  $r = 150$  pc (Leroy et al. 2015). This large reservoir of molecular gas enables active star formation (Sakamoto et al. 2006, 2011; Bolatto et al. 2013; Krieger et al. 2019; Rico-Villas et al. 2020), which affects the properties of molecular gas (e.g., through heating Mangum et al. 2019). The gas in the bar orbit ( $x_1$  orbits) is being fed to the center of NGC 253 ( $x_2$  orbits), and shocks are expected when this gas flow collides with the nuclear ring as discussed above for other galaxies. Figure 1(left) shows IRAC  $8\mu\text{m}$  (Dale et al. 2009; LVL team 2009) and  $\text{CO}(2-1)$  integrated-intensity (ALMA data 2018.1.01321.S; PI: Faesi) images covering most of NGC 253 to indicate the locations of these orbits. The association between shocks at orbital intersections and the chemistry has been proposed by García-Burillo et al. (2000) and Meier et al. (2015).

At the center of NGC 253, a large number of molecular species are detectable (Martín et al. 2006; Meier et al. 2015). To fully explore the chemical complexity in this galaxy, we conducted the ALMA large program ALMA Comprehensive High-resolution Extragalactic Molecular Inventory (ALCHEMI; Martín et al. 2021). ALCHEMI

<sup>1</sup> Bars lie on the  $x_1$  orbits, while  $x_2$  orbits form inner nuclear rings. The location of nuclear rings may correspond to that of inner Lindblad resonances, but this is not always the case (Kim et al. 2012).

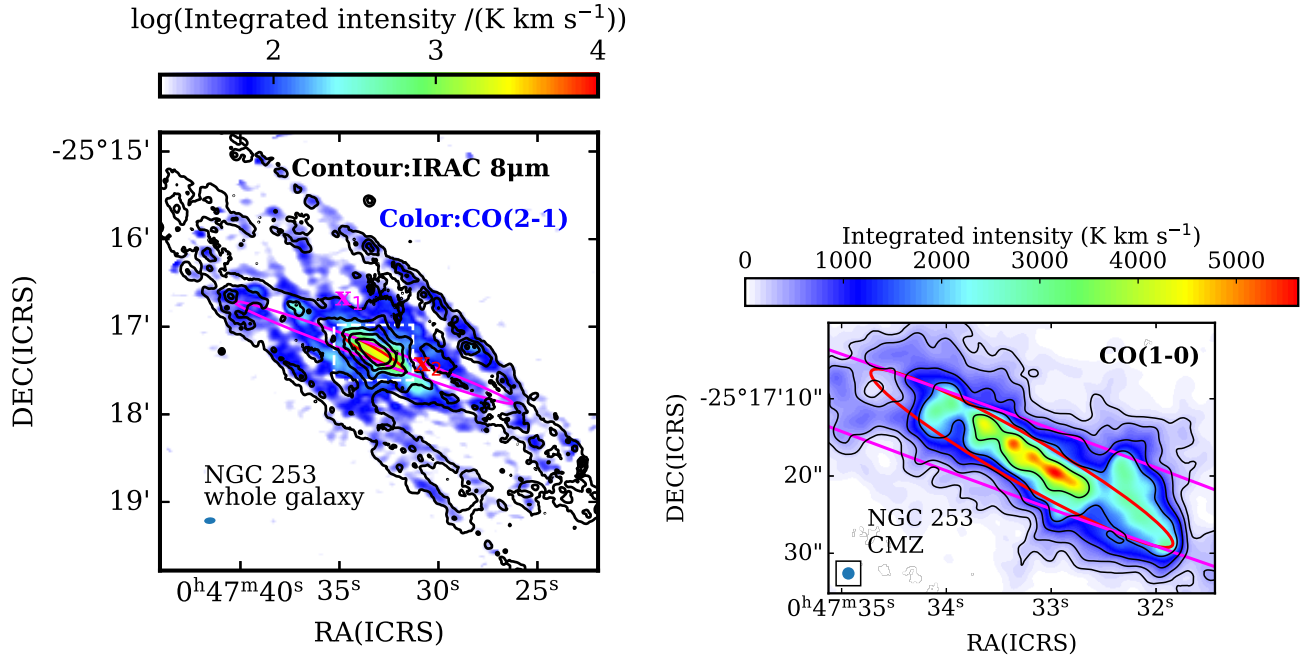


**Figure 1.** (Left) The IRAC 8 $\mu$ m image is shown with contours, while the integrated-intensity image of CO(2-1) is shown with color in the logarithmic scale. The contour levels are 25, 50, 100, 200, and 500 MJy/sr. Approximate positions of bar orbits ( $x_1$  orbits) and inner orbits that form the CMZ ( $x_2$  orbits) are shown with magenta and red ellipses, respectively. The beam size is shown as a blue ellipse on the left-bottom corner. The area shown in Figure 2 and the right panel are indicated with a white dashed rectangle in Figure 2 (left). For more detailed orbit models, we refer readers to other works (e.g., Sorai et al. 2000; Das et al. 2001; Levy et al. 2022). (Right) The integrated intensity image of CO(1-0) overlaid with the same orbits as the left panel.

is a wide-frequency, unbiased spectral scan mosaic toward the CMZ of NGC 253 at a common  $1.6''$  resolution. This survey has discovered high cosmic-ray ionization rates (Holdship et al. 2021; Harada et al. 2021; Holdship et al. 2022), detected a phosphorus-bearing species for the first time in an extragalactic source (Haasler et al. 2022), and detected methanol masers (Humire et al. 2022) in the CMZ of NGC 253. We utilize the ALCHEMI data to study multiple transitions of  $\text{HOCO}^+$ .

This paper is organized as follows. Section 2 describes our observational parameters and data analysis, and images of integrated intensities are presented in Section 3. Derived column densities of  $\text{HOCO}^+$  are shown in Section 4, while the  $\text{HOCO}^+/\text{CO}_2$  ratios are discussed using chemical models in Section 5. In Section 6, we discuss our results including a comparison with ice abundances. Our results are summarized in Section 7.

## 2. OBSERVATIONS AND DATA ANALYSIS

The ALCHEMI spectral survey mosaic of the NGC 253 CMZ was performed between 2017 and 2019, with ALMA 12m-antenna and 7m-antenna arrays. It covered a broad frequency range between 84 and 373 GHz (Bands 3 to 7, avoiding deep atmospheric lines), down to sensitivities  $\sim 10$  mK per  $10 \text{ km s}^{-1}$  channel. The ALCHEMI data products have a uniform angular resolution of  $1''.6$  and cover a field of view of  $50'' \times 20''$  centered on the CMZ of NGC 253 (phase center  $\alpha = 00^{\text{h}}47^{\text{m}}33.28^{\text{s}}$ ,  $\delta = -25^{\circ}17'17.7''$  (ICRS)). The extent of the largest recoverable angular scale is greater than or equal to  $15''$ . A detailed description of the ALCHEMI survey products can be found in Martín et al. (2021).

We extracted the line cubes around the transitions of  $\text{HOCO}^+$  with a velocity resolution binned to  $10 \text{ km s}^{-1}$ . Within the  $\sim 290$  GHz coverage of the ALCHEMI survey, we find 14 detectable  $\text{HOCO}^+$  transitions, occurring every  $\sim 21.4$  GHz. However, some transitions are severely blended with transitions from other species and are not used in this analysis. The spectroscopic parameters and spectral channel RMS values for the  $\text{HOCO}^+$  transitions used in this paper are listed in Table 1.

## 3. INTEGRATED INTENSITIES

Figure 2 (a-d) shows the velocity-integrated intensity (moment 0) images of  $\text{HOCO}^+$  in multiple transitions (see Table 1 for their properties). Many transitions used in this work have neighboring lines, and it is not possible to make the moment 0 images simply by collapsing neighboring channels. To exclude this contamina-

tion, we applied the 3-D mask made from the position-position-velocity space only including pixels with  $\text{CO } J = 1 - 0$  detections above the  $20\sigma$  level. The  $20\sigma$  cut-off may sound unnecessarily high, but the signal-to-noise ratios of  $\text{HOCO}^+$  transitions are more than 100 times lower than that of  $\text{CO}(1-0)$ . Therefore, this mask does not exclude any notable  $\text{HOCO}^+$  emission but helps to exclude the contamination from nitrogen sulfide transitions neighboring with  $\text{CO}(1-0)$  to be included in the mask. Despite the elimination of contamination with this mask, the only transition that is free from contamination is  $5_{0,5} - 4_{0,4}$  (panel a) of Figure 2. Other images that are relatively less affected from blending are also shown in Figure 2 (panels b-d). The level of contamination is usually very low ( $< 10\%$ ) except for GMC 5, where there is little  $\text{HOCO}^+$  emission and stronger emission from neighboring lines. Transitions  $4_{0,4} - 3_{0,3}$  and  $8_{0,8} - 7_{0,7}$  can still be used to obtain column densities as we use spectral fitting, but their images are not shown. A low-excitation line of  $\text{HOCO}^+$  ( $5_{0,5} - 4_{0,4}$ ;  $E_{\text{up}} = 15.4 \text{ K}$ ) shows peaks near the outer CMZ, in giant molecular clouds (GMCs) 1, 7, and 9 (GMC numbering is shown in panel f; Leroy et al. 2015, see also Appendix C for coordinates). On the other hand, the higher-excitation transitions ( $E_{\text{up}} \gtrsim 30 \text{ K}$ ) peak closer to the center (GMCs 3 and 6).

Panels (e) and (f) of Figure 2 show integrated-intensity images of  $\text{CH}_3\text{OH}(2_k - 1_k)$  (group of transitions at  $\nu_{\text{rest}} \sim 96.74$  GHz with the strongest transition  $2_0^+ - 1_0^+$ )<sup>2</sup> and  $\text{H}^{13}\text{CO}^+(1-0)$  ( $\nu_{\text{rest}} = 86.75$  GHz) for comparison. The emission distribution of  $\text{CH}_3\text{OH}(2_k - 1_k)$  is similar to that of the low- $J$  transitions of  $\text{HOCO}^+$ , as well as low- $J$  transitions of  $\text{HNCO}$ , and  $\text{SiO}$  (Meier et al. 2015, Huang et al., in preparation). On the other hand, the distribution of  $\text{H}^{13}\text{CO}^+(1-0)$ , which is rather similar to that of molecules with strongest emission (e.g.,  $\text{CO}$ ,  $\text{HCO}^+$ ,  $\text{HCN}$ ,  $\text{CS}$ , etc. Meier et al. 2015; Martín et al. 2021), is clearly different from that of  $\text{HOCO}^+$ . The  $\text{H}^{13}\text{CO}^+(1-0)$  emission is concentrated near the center of NGC 253 (GMCs 3-7) instead of the outer CMZ.

The similarity between integrated intensities of  $\text{HOCO}^+$  ( $5_{0,5} - 4_{0,4}$ ) and  $\text{CH}_3\text{OH}(2_k - 1_k)$  and the difference between those of  $\text{HOCO}^+$  ( $5_{0,5} - 4_{0,4}$ ) and  $\text{H}^{13}\text{CO}^+(1-0)$  are highlighted in Figure 3. While the  $\text{HOCO}^+(5_{0,5} - 4_{0,4})/\text{CH}_3\text{OH}(2_k - 1_k)$  ratios are relatively constant, the  $\text{HOCO}^+(5_{0,5} - 4_{0,4})/\text{H}^{13}\text{CO}^+(1-0)$  ratio varies significantly. All these transitions have relatively low upper state energies ( $\text{HOCO}^+(5_{0,5} - 4_{0,4})$ :

<sup>2</sup> These transitions may not be in local thermodynamic equilibrium (LTE), but are “quasi thermal” and they are not identified as masing (Humire et al. 2022).

**Table 1.** HOCO<sup>+</sup> Spectroscopic Properties and RMS Noise Values

Transition	$\nu_{rest}^{(a)}$ (GHz)	$E_{up}^{(b)}$ (K)	$\log(A_{ul})^{(c)}$ (s <sup>-1</sup> )	RMS <sup>(d)</sup> (mJy beam <sup>-1</sup> )	RMS <sup>(e)</sup> (mK)	Blending <sup>(f)</sup>
4 <sub>0,4</sub> -3 <sub>0,3</sub>	85.531	10.3	-4.63	0.19	12.	Potential blending with CH <sub>3</sub> CCH. Minor blending with U-lines
5 <sub>0,5</sub> -4 <sub>0,4</sub>	106.914	15.4	-4.33	0.20	8.4	N/A
6 <sub>0,6</sub> -5 <sub>0,5</sub>	128.295	21.6	-4.08	0.33	9.5	Minor blending with U-lines
7 <sub>0,7</sub> -6 <sub>0,6</sub>	149.676	28.7	-3.88	0.42	9.0	Potential blending with U-lines
8 <sub>0,8</sub> -7 <sub>0,7</sub>	171.056	36.9	-3.70	0.75	12.	Potential blending with CH <sub>3</sub> CCH.
12 <sub>0,12</sub> -11 <sub>0,11</sub>	256.566	80.0	-3.16	0.99	7.2	Potential blending with CH <sub>3</sub> CCH, HC <sub>3</sub> N $v_7 = 2$
Transitions below were not used for analysis						
9 <sub>0,9</sub> -8 <sub>0,8</sub>	192.435	46.2	-3.54			Blended with U-line
10 <sub>0,10</sub> -9 <sub>0,9</sub>	213.813	56.4	-3.40			Blended with C <sub>2</sub> H <sub>5</sub> OH
11 <sub>0,11</sub> -10 <sub>0,10</sub>	235.190	67.7	-3.28			Blended with SO <sub>2</sub>
13 <sub>0,13</sub> -12 <sub>0,12</sub>	277.941	93.4	-3.06			Blended with U-line
14 <sub>0,14</sub> -13 <sub>0,13</sub>	299.314	107.7	-2.96			Non detection
15 <sub>0,15</sub> -14 <sub>0,14</sub>	320.686	123.1	-2.87			Non detection
16 <sub>0,16</sub> -15 <sub>0,15</sub>	342.056	139.6	-2.78			Non detection
17 <sub>0,17</sub> -16 <sub>0,16</sub>	363.424	157.0	-2.70			Non detection

NOTE—(a) Rest frequency; (b) Upper level energy of the transition; (c)  $A_{ul}$ : Einstein coefficient of spontaneous emission. All values were taken from the Cologne Database for Molecular Spectroscopy (CDMS; <https://cdms.astro.uni-koeln.de>; Müller et al. 2001, 2005; Bizzocchi et al. 2017); (d) and (e) RMS values of a single channel with  $\Delta v = 10 \text{ km s}^{-1}$  in mJy beam<sup>-1</sup> and mK units; (f) presence of blending; Transitions are shown with quantum numbers  $J_{K_a, K_c}$ . Only  $K_a = 0$  transitions are shown because transitions with  $K_a \neq 0$  are not detected due to their higher energy state and lower Einstein coefficients. The upper part of this table shows transitions used for the analyses of this paper, whose line shapes are separable from neighboring lines. The lower part lists transitions with severe blending or without reliable detection. “Potential blending” means the case where the line centers are separated by more than  $200 \text{ km s}^{-1}$ , but the line wing can contaminate the moment maps of HOCO<sup>+</sup> transitions.

$E_u = 15.4 \text{ K}$ , CH<sub>3</sub>OH ( $2_0^+ - 1_0^+$ ):  $E_u = 7.0 \text{ K}$ , H<sup>13</sup>CO<sup>+</sup> ( $1-0$ ):  $E_u = 4.2 \text{ K}$ ), and these ratio maps should be good proxies for variations in column densities of these molecules.

#### 4. COLUMN DENSITIES AND FRACTIONAL ABUNDANCES

Figure 4(a) shows the column density map of HOCO<sup>+</sup>. These column densities were derived using the public software CASSIS (<http://cassis.irap.omp.eu/>; Vastel et al. 2015) supplied with spectroscopic constants from the spectroscopic database from the CDMS (Müller et al. 2001, 2005). CASSIS calculates molecular column densities based on input spectral line brightness temperatures with consideration of optical depths, either with an LTE assumption or, if collisional rates are available, non-LTE assumption. We used a Markov Chain Monte Carlo (MCMC) algorithm assuming LTE to fit column densities, excitation temperatures, line velocities, and line widths (see Appendix A). Column densities were calculated only for the pixels with  $> 3\sigma$  detection of both HOCO<sup>+</sup>(4<sub>0,4</sub> – 3<sub>0,3</sub>) and HOCO<sup>+</sup>(5<sub>0,5</sub> – 4<sub>0,4</sub>) at

velocities within  $30 \text{ km s}^{-1}$  from the line center. Line-center velocities used for this  $3\text{-}\sigma$  detection criterion are determined from the image cube of CO(1-0) from ALCHEMI data. These line-center velocities from CO may be different from HOCO<sup>+</sup> velocities fitted from CASSIS. Instead of deriving the column densities and excitation temperatures on a pixel-by-pixel basis, we bin the intensities within hexagonal pixels with a horizontal length of  $0''.8$ , half of the image spatial resolution of  $1.6''$ , to reduce the computational time running CASSIS. Examples of spectral fitting are shown for hexagonal pixels located at  $(x_{\text{offset}}, y_{\text{offset}}) = (-17.3'', -10.4'')$  and  $(2.0'', 2.1'')$  in Figure 5 where the offset is taken from the phase center. In general, the observed spectra fit well with the LTE spectra. The resulting column-density distribution appears similar to that of the moment 0 images of low-excitation transitions (e.g., Figure 2a).

Excitation temperatures derived from the above spectral fitting are shown in Figure 4(b). While regions far

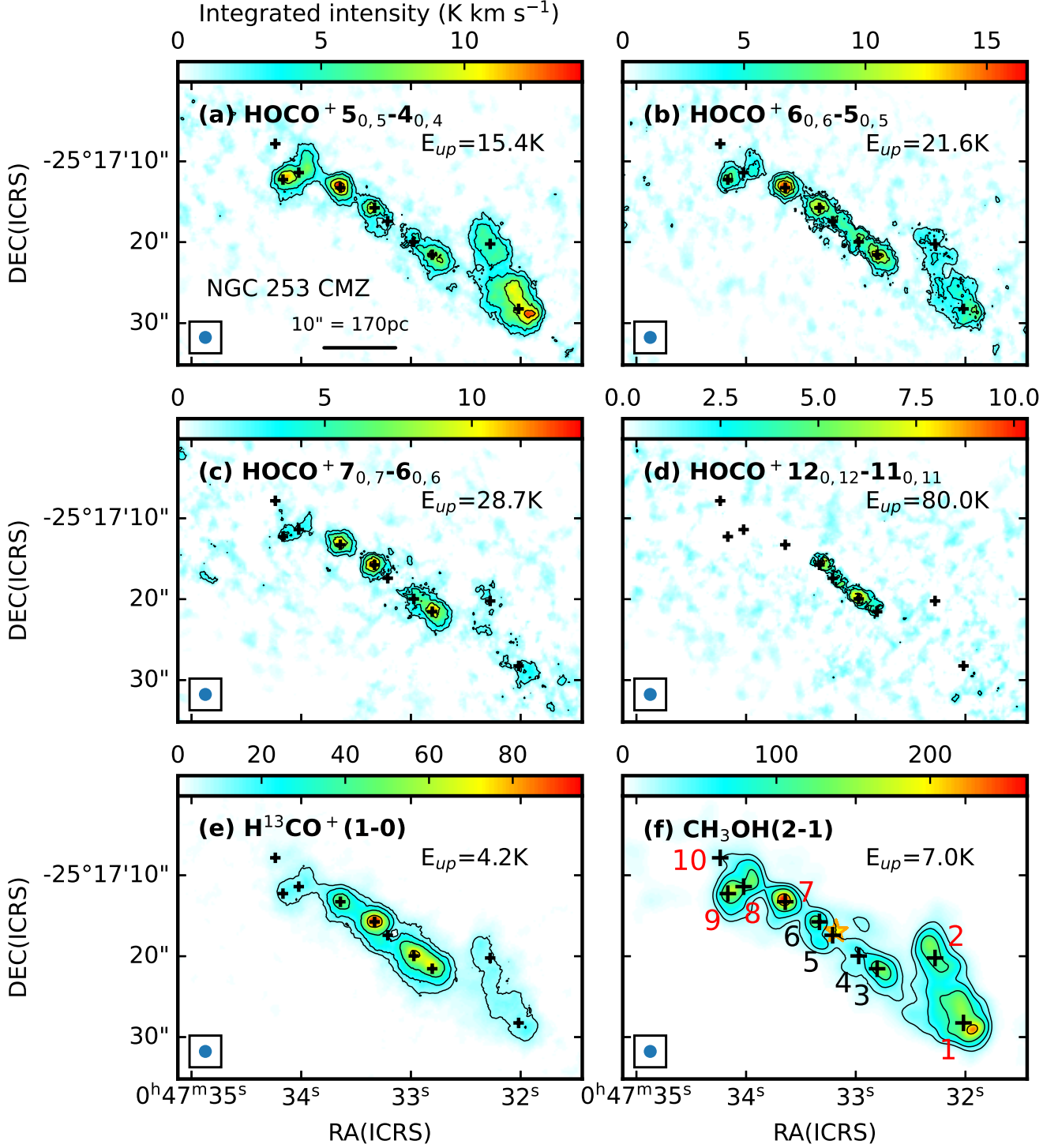


**Figure 2.** Velocity-integrated intensity maps of (a-d) four HOCO<sup>+</sup> transitions, (e) H<sup>13</sup>CO<sup>+</sup>(1-0), and (f) CH<sub>3</sub>OH(2<sub>k</sub> - 1<sub>k</sub>). Contour levels are (a-d) [2, 4, 8, 12], (e) [9.0, 18.0, 36.0, 72.0], and (f) [25.0, 50.0, 100.0, 200.0] K km s<sup>-1</sup>. The beam size of 1.6" × 1.6" (27 pc × 27 pc) is shown at the bottom left corner in each panel as a blue circle. Locations of GMCs identified by Leroy et al. (2015) are shown as black crosses and labeled in panel (f). Coordinates of these GMCs are given in Table 3. The kinematic center known as “TH2” (Turner & Ho 1985) with the revised coordinate by Cohen et al. (2020) is shown as a yellow star with orange edges in panel (f). GMCs with Class I methanol maser detection by Humire et al. (2022) are labeled with red numbers in panel (f).

from the kinematic center<sup>3</sup> of NGC 253 show low excitation temperatures of  $\lesssim 10$  K (GMCs 1, 2, 8, and 9), the excitation temperatures become higher, up to 40 K, near the center of NGC 253 (GMCs 3 and 6).

We also obtain the total hydrogen column densities (Figure 4c) to calculate fractional abundances of HOCO<sup>+</sup> (the HOCO<sup>+</sup> column densities divided by total hydrogen column densities  $N(\text{H}_2)$ ). The total H<sub>2</sub> column densities were derived from the dust continuum image at 361.5 GHz shown by Harada et al. (2021) with the derivation method based on Hildebrand (1983) for pixels above  $3\sigma$  detection. A simplified formula is given as Equation (3) in Mangum et al. (2019):

$$N(\text{H}_2)(\text{cm}^{-2}) \sim 7.0 \times 10^{22} R_{dg} \left( \frac{\lambda(\text{mm})}{0.4} \right)^\beta \frac{T_R(\text{K})}{T_d(\text{K})}, \quad (1)$$

where  $N(\text{H}_2)$  is the molecular hydrogen column density,  $R_{dg}$  is the dust-to-gas mass ratio,  $\lambda$  is the wavelength,  $T_R$  is the radiation temperature, and  $T_d$  is the dust temperature. This formula is valid for  $h\nu \ll kT_d$  (the Rayleigh-Jeans approximation). We use the emissivity  $\beta = 1.5$ , a dust temperature  $T_{\text{dust}} = 30$  K, and a dust-to-gas mass ratio of 150 following Mangum et al. (2019). This estimate of the dust temperature is close to the observed value, but some dust components may be warmer. Pérez-Beaupuits et al. (2018) derived dust temperature components of 37, 70, and 188 K in the central region of NGC 253 using their assumed source size of  $17.3'' \times 9.2''$  from their Herschel and SOFIA observations. These components contain mass fractions of 65, 26, and 9%, respectively. If the dust is warmer, the actual column density should be smaller by a similar factor; for instance, a factor of 5 smaller if  $T_{\text{dust}} = 150$  K. The column-density dependence on the dust temperature becomes larger than  $\propto \frac{1}{T_d}$  when the dust is cold ( $T_d \lesssim 20$  K) and one cannot use the Rayleigh-Jeans approximation, but we expect that there is a very small amount of cold dust in the center of NGC 253.

The fractional abundance of HOCO<sup>+</sup> is higher at larger distances from the center of NGC 253, and it decreases by more than an order of magnitude at the center (Figure 4d). At peaks of HOCO<sup>+</sup> (GMCs 1, 8, and 9), the fractional abundance is  $\sim (1 - 2) \times 10^{-9}$ , similar to those observed in Galactic center clouds:  $(2 - 8) \times 10^{-9}$  (Minh et al. 1991; Armijos-Abendaño et al. 2015). On the other hand, it is orders of magnitude higher than those observed in Galactic disk clouds, which range from

$10^{-13}$  to  $5 \times 10^{-11}$  (Vastel et al. 2016; Fontani et al. 2018; Majumdar et al. 2018).

## 5. HOCO<sup>+</sup>/CO<sub>2</sub> RATIOS

To estimate the gas-phase abundances of CO<sub>2</sub> from HOCO<sup>+</sup>, we ran chemical abundance models based on Nautilus (Ruaud et al. 2016), accounting for gas, ice surface, and ice mantle phases. In addition to the thermal evaporation, desorption from dust heating due to cosmic rays (Hasegawa & Herbst 1993) is included in the model. Desorption through cosmic-ray heating of dust is where the dust grain is temporarily heated to a certain maximum temperature for a very short time scale ( $\sim 10^{-5}$  s), then cools down. The model also includes photodesorption (Öberg et al. 2009b,a) both from direct UV photons and cosmic-ray-induced UV photons with a default yield of  $10^{-4}$  for all the grain species. We also ran a model with a desorption yield of  $10^{-3}$  for CO<sub>2</sub>. Our models do not include shocks. We calculated grid models with varying densities ( $n = 10^3 - 10^6 \text{ cm}^{-3}$ ) and cosmic-ray ionization rates ( $\zeta = 10^{-17} - 10^{-12} \text{ s}^{-1}$ ) following a similar approach as Harada et al. (2021). Temperatures were calculated in the Meudon Photodissociation Region (PDR) code (ver. 1.5.4) (Le Petit et al. 2006) (Figure 6a), and were fed to Nautilus to run chemical abundance models with a larger chemical network. Despite the high gas temperature with the high cosmic-ray ionization rate ( $T > 1000$  K when  $\zeta = 10^{-12} \text{ s}^{-1}$  and  $n = 10^3 \text{ cm}^{-3}$ ), the dust temperature calculated from the Meudon code remains cold, around 11 K. We adopted a maximum visual extinction  $A_V = 20$  mag with a turbulent velocity of  $1 \text{ km s}^{-1}$ , and used the temperature in the model at  $A_V = 10$  mag (Figure 6d), where the effects of the PDRs are negligible. We note that, unlike in the description of observational results, fractional abundances are expressed as abundances of certain species over total hydrogen abundances ( $N_{\text{Htotal}} = N_{\text{Hatom}} + 2N_{\text{H}_2}$ ), instead of molecular hydrogen abundances.

Figure 6 (b) shows HOCO<sup>+</sup>/CO<sub>2</sub> abundance ratios in the gas phase, that vary between  $10^{-5} - 10^{-2}$  for the most part. Previous ALCHEMI studies have suggested that the cosmic-ray ionization rates in NGC 253 are at least a few orders of magnitude higher than that in the Galactic spiral arm clouds (Holdship et al. 2021; Harada et al. 2021; Holdship et al. 2022), which increases the HOCO<sup>+</sup>/CO<sub>2</sub> abundance ratios due to an increased H<sub>3</sub><sup>+</sup> abundance. Although the cosmic-ray ionization rates are expected to be high, extremely high rates ( $\zeta \gtrsim 10^{-13} \text{ s}^{-1}$  for  $n = 10^5 \text{ cm}^{-3}$ ) would destroy HOCO<sup>+</sup> (Figure 6c), especially in lower density regions. Therefore, we consider HOCO<sup>+</sup>/CO<sub>2</sub> ratios of  $\sim 10^{-3} - 10^{-2}$  in later sections, which are taken from

<sup>3</sup> The kinematic center of NGC 253 is located near GMC 5 (Turner & Ho 1985; Müller-Sánchez et al. 2010). Although there is a debate on the exact location of the kinematic center, the difference of  $0''.7$  appearing in the literature does not affect our discussion.

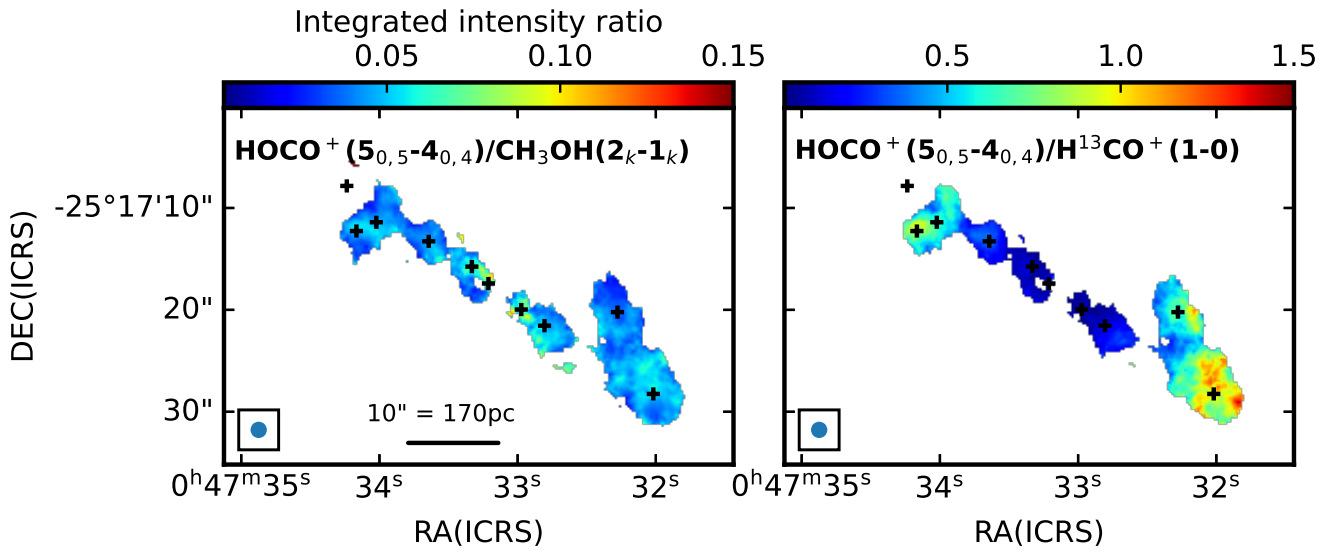


**Figure 3.** Integrated intensity ratios of (left)  $\text{HOCO}^+(5_{0,5}-4_{0,4})/\text{CH}_3\text{OH}(2_k-1_k)$  and (right)  $\text{HOCO}^+(5_{0,5}-4_{0,4})/\text{H}^{13}\text{CO}^+(1-0)$ . Only pixels with integrated intensity of  $> 3\sigma$  for each transition and ratio are shown. Ranges of color scales are set to be 0.003-0.15 (left) and 0.03-1.5 (right), respectively. Because the maximum/minimum ratios of color scales are 50 for both images, variations in color scales between the left and right panels represent variations in the  $\text{HOCO}^+(5_{0,5}-4_{0,4})/\text{CH}_3\text{OH}(2_k-1_k)$  and  $\text{HOCO}^+(5_{0,5}-4_{0,4})/\text{H}^{13}\text{CO}^+(1-0)$  ratios.



the parameter space where the HOCO<sup>+</sup> abundance is moderately high<sup>4</sup>.

It is worth noting that cosmic-ray-induced desorption mechanisms do not change the abundances significantly. This is because cosmic-ray-induced photodissociation is a more efficient form of destruction than desorption if the desorption yield is on the order of 10<sup>-3</sup> or lower. According to Öberg et al. (2009b), the photodesorption yield of CO<sub>2</sub> cannot go higher than a few times 10<sup>-3</sup>, which means photodesorption is not significant. Desorption of CO<sub>2</sub> due to cosmic-ray heating of dust has an even lower effect than the photodesorption for models run with the commonly-used maximum dust temperature of 70 K.

In our model, the dominant formation reactions of HOCO<sup>+</sup> vary with time. In general, protonation of CO<sub>2</sub> is more dominant in early time (< 10<sup>5</sup> yr), and the gas-phase production with HCO<sup>+</sup> and OH becomes more efficient in later times (see Section 1). However, the dominant formation routes also vary with physical conditions and it is difficult to conclude which one is more dominant.

Although our models do not include shocks, but we argue that this approach should be sufficient to estimate the HOCO<sup>+</sup>/CO<sub>2</sub> ratios, especially their upper limit. The HOCO<sup>+</sup>/CO<sub>2</sub> ratios are determined by the balance among the protonation of CO<sub>2</sub>, electron recombination of HOCO<sup>+</sup>, proton transfer from HOCO<sup>+</sup> to species with higher proton affinity than CO<sub>2</sub>, and the ion-neutral production of HOCO<sup>+</sup> (HCO<sup>+</sup> + OH). These reactions occur regardless of shocks. If shocks evaporate CO<sub>2</sub> significantly, there should be less contribution from the HOCO<sup>+</sup> formation through HCO<sup>+</sup> and OH compared with the protonation of CO<sub>2</sub>, and the HOCO<sup>+</sup>/CO<sub>2</sub> ratios should be lower, while shocks should increase the fractional abundances of both HOCO<sup>+</sup> and CO<sub>2</sub>. Therefore, our models without shocks are likely sufficient to obtain upper limits of the HOCO<sup>+</sup>/CO<sub>2</sub> ratios, but more realistic modeling with shocks will be conducted as future work. It should also be noted that the models without shocks severely underproduce HOCO<sup>+</sup> fractional abundances compared with observed peak values, which implies the need for shocks to explain the observed abundances (see Section 6.1). We include the gas-neutral reaction of HCO<sup>+</sup> + OH and many other related reactions in the model. The fact that

our model could not reproduce the observed fractional abundances suggests that the formation route through this reaction is not enough to explain our observations.

## 6. DISCUSSION

### 6.1. *Origins of HOCO<sup>+</sup> emission*

As discussed earlier, the formation routes of HOCO<sup>+</sup> do not have to involve the protonation of CO<sub>2</sub>. The gas-phase reaction between HCO<sup>+</sup> and OH may also contribute to HOCO<sup>+</sup>. Fontani et al. (2018) argued that HOCO<sup>+</sup> must be formed via the reaction above (HCO<sup>+</sup> + OH; see Sect. 1) in high-mass star-forming cores because HOCO<sup>+</sup> fractional abundances derived from the 4<sub>0,4</sub> – 3<sub>0,3</sub> transition are correlated with the fractional abundances of H<sup>13</sup>CO<sup>+</sup>, while there is no correlation with that of methanol. If HOCO<sup>+</sup> is formed via protonation, a large amount of evaporated CO<sub>2</sub> must be present, which also implies a large amount of methanol in the gas phase. This is because methanol is formed on the ice, and its gas-phase production is extremely inefficient (Garrod et al. 2007).

The CMZ of NGC 253 shows a different trend from the case of these high-mass star-forming cores. We do see a positive spatial correlation between HOCO<sup>+</sup> and CH<sub>3</sub>OH with low-excitation transitions of both molecules enhanced at the outer CMZ of NGC 253 (Figure 3). Meanwhile, the correlation between HOCO<sup>+</sup> and H<sup>13</sup>CO<sup>+</sup> is weak because H<sup>13</sup>CO<sup>+</sup> is more abundant near the center of the CMZ (Figure 3; see also Harada et al. 2021, for abundances of H<sup>13</sup>CO<sup>+</sup>). There is a caveat that the ice composition may be different in high-mass star-forming regions observed by Fontani et al. (2018) and NGC 253 CMZ, and the presence or lack of correlation may not necessarily imply a difference in formation routes. On the other hand, the presence of a correlation between CH<sub>3</sub>OH and HOCO<sup>+</sup> and the lack of correlation between HOCO<sup>+</sup> and most other species (e.g., CO, HCN, HCO<sup>+</sup>, etc.) strongly suggest a similar mechanism enhancing abundances of both CH<sub>3</sub>OH and HOCO<sup>+</sup>. This mechanism must involve desorption, as methanol is only efficiently formed on ice. Therefore, we argue that HOCO<sup>+</sup> in our observations is likely formed from CO<sub>2</sub> through protonation.

### 6.2. *Inferred gas-phase CO<sub>2</sub> fractional abundances*

If HOCO<sup>+</sup> is produced through the protonation of CO<sub>2</sub> as we discussed above, CO<sub>2</sub> must be evaporated from ice into the gas phase because CO<sub>2</sub> is much more abundant in the ice than in the gas phase (Figure 6d). Obtaining the gas-phase fractional abundances of CO<sub>2</sub> could provide essential hints helping us to evaluate the origin of the gas-phase CO<sub>2</sub>. From the chemical model,

<sup>4</sup> We note that the presence of HOCO<sup>+</sup> is still consistent with the cosmic-ray ionization rates derived by Holdship et al. (2021) and Harada et al. (2021) ( $\zeta \gtrsim 10^{-14} \text{ s}^{-1}$  for  $n = 10^5 \text{ cm}^{-3}$ ), but the value obtained by Holdship et al. (2022) ( $\zeta \sim 10^{-13} \text{ s}^{-1}$  for  $n = 10^5 \text{ cm}^{-3}$ ) would not allow high fractional abundances of HOCO<sup>+</sup>.

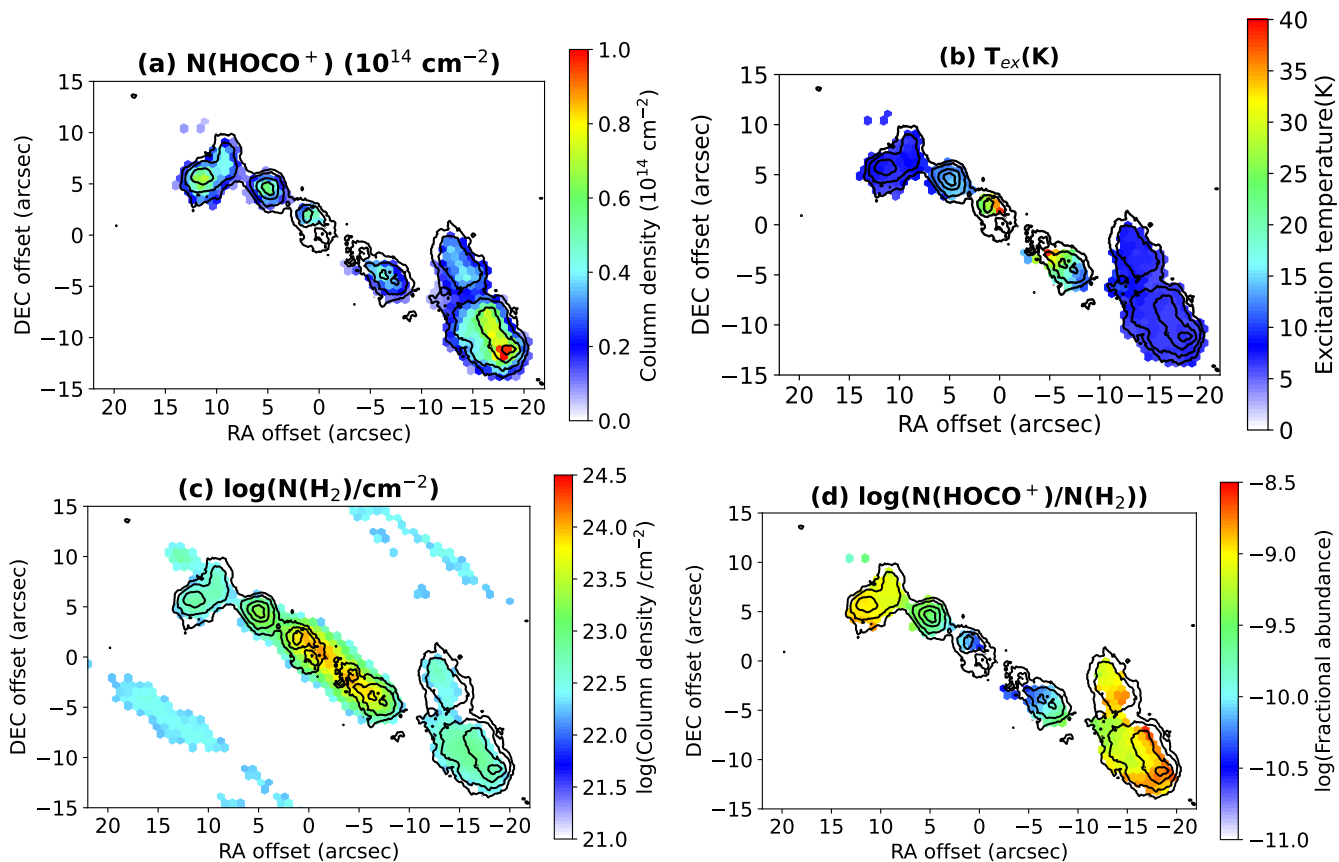


**Figure 4.** Maps of (a) the HOCO<sup>+</sup> column density, (b) the excitation temperature of HOCO<sup>+</sup> derived from CASSIS, (c) the total H<sub>2</sub> column density derived from the dust continuum shown in a logarithmic scale, and (d) the fractional abundance of HOCO<sup>+</sup> shown in the logarithmic scale. The black contours show HOCO<sup>+</sup> (5<sub>0,5</sub> - 4<sub>0,4</sub>) integrated intensities as in Figure 2.

we find that the range of the HOCO<sup>+</sup>/CO<sub>2</sub> ratio is  $\sim 0.001 - 0.01$ . Because the maximum fractional abundance of HOCO<sup>+</sup> is  $\sim 2 \times 10^{-9}$  in GMC 1 and  $\sim 1 \times 10^{-9}$  in GMCs 2, 8, and 9, the gas-phase CO<sub>2</sub> fractional abundances can be  $(1 - 20) \times 10^{-7}$  at the outer CMZ, where the HOCO<sup>+</sup> intensity peaks.

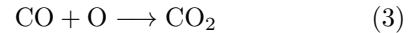
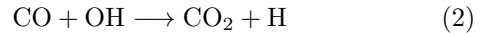
### 6.3. Comparison with ice observations of CO<sub>2</sub>

Here we compare the fractional abundance of CO<sub>2</sub> gas estimated above with that of CO<sub>2</sub> ice observations. We utilize the CO<sub>2</sub> column densities of selected regions of AKARI observations by Yamagishi et al. (2015). Although this reference describes these observations in detail, we include the summary of them in Appendix B. These observations used a rectangle slit with a size of  $5'' \times 5.8''$  (Fig 7 left). Subsequently, we extracted the values of the continuum flux from the same regions to estimate the total H<sub>2</sub> column density using the method described in Section 4. We then derived the fractional abundances of CO<sub>2</sub> in the ice phase in these regions shown in Figure 7 (right). We note that the components traced with CO<sub>2</sub> ice likely come from relatively lower-column-density regions than the ones traced by the dust continuum. Therefore, we have to be aware of the caveat that our estimation of the CO<sub>2</sub> fractional abundances is rather crude, only accurate for an order of magnitude approximation.

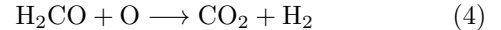
The CO<sub>2</sub> ice fractional abundances near the center of NGC 253 (rectangular regions 2 and 3) are lower than in regions 4 and 5 by about an order of magnitude or more. Away from the center, the CO<sub>2</sub> ice fractional abundances are similar to those of the Milky Way ISM of  $\sim 10^{-6} - 10^{-5}$  (Boonman et al. 2003), which is also consistent with fractional abundances of CO<sub>2</sub> ice in our chemical model. Therefore, the CO<sub>2</sub> ice abundance decreases towards the center of NGC 253, deviating from the Milky Way value. We note that, if we use a higher dust temperature, we would derive lower H<sub>2</sub> column densities than those we show in Figure 4. Subsequently, the fractional abundance estimate would increase. Although the warm dust does not fully explain the large difference in the derived fractional abundances between the outer part (rectangular regions 4 and 5) and center (rectangular regions 2 and 3) of the CMZ, this uncertainty should be considered in the interpretation of the data.

If the CO<sub>2</sub> ice fractional abundance is indeed lower in the center than at the outer CMZ, one of the possible factors that may attribute to this suppression is photodissociation, either directly by UV photons or cosmic-ray-induced UV photons. Because of the high star formation rate in the rectangular regions 2 and 3, strong photodissociation is expected (Meier et al. 2015).

Warm dust can also lower the ice abundance of CO<sub>2</sub> through desorbing CO<sub>2</sub> ice into the gas phase, or desorbing the precursors of CO<sub>2</sub> ice. Desorption of many CO<sub>2</sub> precursors can take place with lower dust temperatures than the desorption of CO<sub>2</sub> itself. CO<sub>2</sub> ice is thought to be formed through



(Minissale et al. 2013) and possibly



(Minissale et al. 2015). Some of these reactants have lower binding energies than CO<sub>2</sub> ( $E_b(\text{CO}_2) \sim 3000$  K,  $E_b(\text{CO}) \sim 1300$  K,  $E_b(\text{O}) \sim 1600$  K; Wakelam et al. 2017; Minissale et al. 2022)<sup>5</sup>. Higher dust temperatures increase the desorption rates of ice species, and species with lower binding energies can desorb with lower dust temperatures (35-50 K for CO,  $\sim 50$  K for O,  $\sim 80$  K for CO<sub>2</sub> Minissale et al. 2022). If a desorption rate of any of these reactants is faster than the reaction rate to form CO<sub>2</sub> there would be less abundances of CO<sub>2</sub> ice. Although the mass of warm or hot dust is smaller than that of cold dust, these warm/hot components are likely concentrated in rectangular regions 2 and 3 in Figure 7 where the star formation is active. This can explain the suppression of ice in these regions as well as low HOCO<sup>+</sup> fractional abundances in GMCs 4 and 5 (see Figure 2f).

Cosmic rays could also contribute to ice desorption. We argued in Section 5 that cosmic-ray-induced desorption is likely negligible, but its effect could possibly be enhanced in NGC 253. Hasegawa & Herbst (1993) estimated that the maximum dust temperature due to the cosmic ray heating of the dust is 70 K, but this temperature can be different for the case of NGC 253, where some dust is already warm. With the higher maximum dust temperature, the evaporation rate of ice species can be enhanced (e.g., Kalvāns & Kalnin 2020). This dependence of desorption due to cosmic-ray heating on the dust temperature should be further explored with theoretical studies.

Variation of the CO<sub>2</sub> ice abundance can be also caused by the initial ice composition. For example, the ice may be rich in atomic or molecular hydrogen. If the

<sup>5</sup> Note that the binding energy is not the temperature where desorption takes place. Effects of desorption appear when the desorption rate becomes significant enough compared with the accretion rate. There is also an additional complication caused by the ice composition. For example, even if a species has a low binding energy, it may not desorb if it is buried in the ice of another species with a higher binding energy.

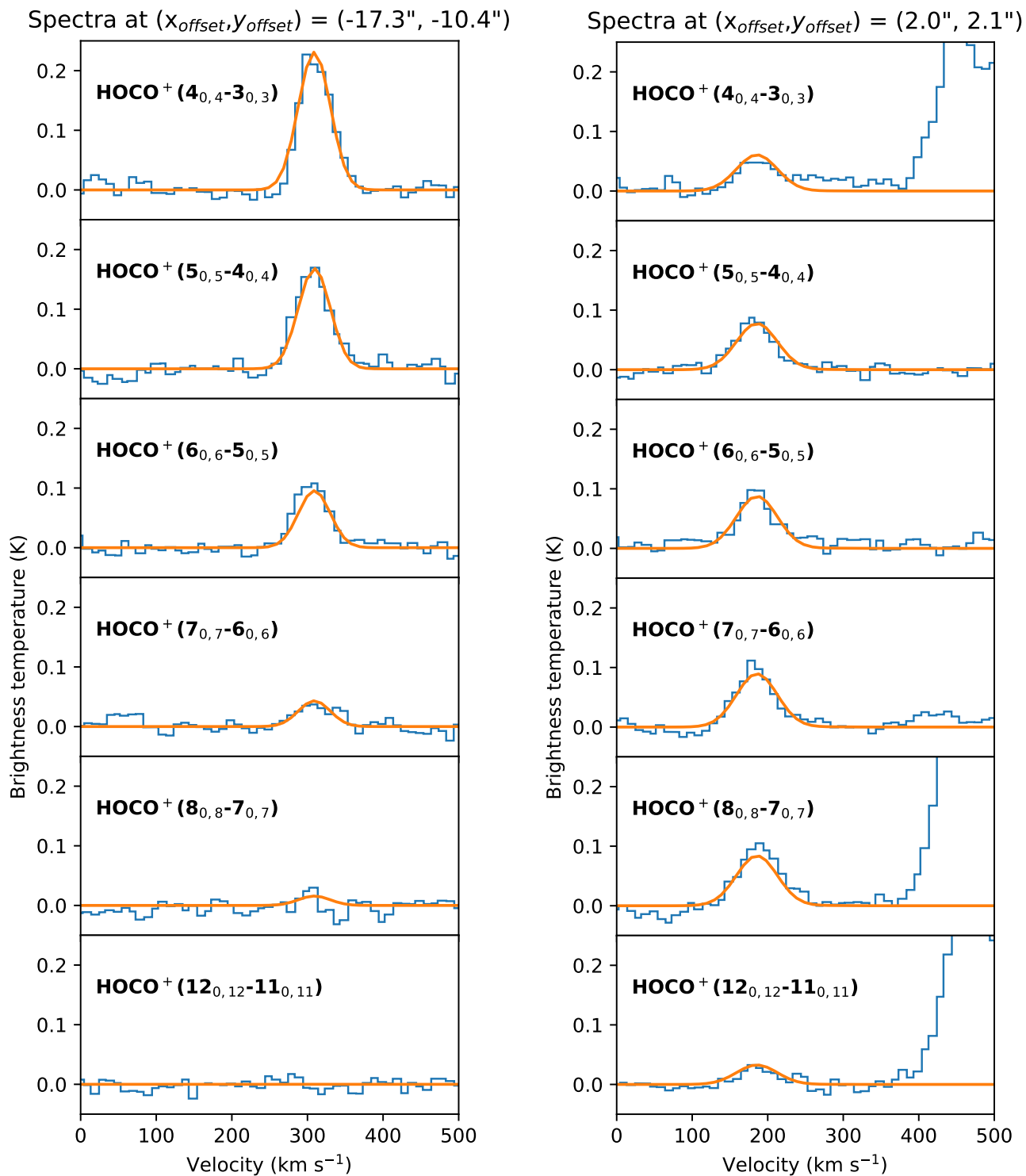


**Figure 5.** Examples of observed spectra (blue) versus modeled spectra by CASSIS (orange) at  $(x_{\text{offset}}, y_{\text{offset}})$  of (Left Panel)  $(-17.3'', -10.4'')$  and (Right Panel)  $(2.0'', 2.1'')$  relative to the phase center of our observations.

ice is abundant in atomic H, frequent hydrogenation reactions can occur, and species such as water, CH<sub>4</sub>, NH<sub>3</sub>, and CH<sub>3</sub>OH may be abundant. On the other hand, if atomic H is deficient, CO<sub>2</sub> formation may be a more dominant route of destroying CO ice than CH<sub>3</sub>OH formation. Although it is difficult to assess how much the ice compositions differ between Galactic star-forming regions and NGC 253 CMZ, we note that this is another factor that could affect the overall chemistry.

#### 6.4. Ice and gas-phase chemistry in NGC 253

We find that the gas-phase fractional abundance of CO<sub>2</sub> can be  $\sim (1 - 20) \times 10^{-7}$  in GMCs 1, 2, 8, and 9 (Section 6.2), and the ice fractional abundance is  $\sim 2 \times 10^{-6}$  around GMC 1 (rectangular region 5 in Figure 7). This means that there is a process sublimating a large fraction of CO<sub>2</sub> ice into the gas phase in these GMCs.

One possible CO<sub>2</sub> sublimation mechanism is a hydrodynamical shock. Chemical models have shown that shocks can sputter off the ice because some gas particles have enough kinetic energy to desorb ice (Jiménez-Serra et al. 2008; Viti et al. 2011; Flower & Pineau des Forêts 2012). We also note that shock sublimation occurs even when the dust temperature is low, because the energy is provided by gas. When the shock velocity is high  $> 20 \text{ km s}^{-1}$ , ice sputtering is efficient enough to desorb a large fraction of ice (Harada et al. 2015). Ubiquitous methanol emission is likely attributed to shock sublimation in the Milky Way Galactic Center (Menten et al. 2009), and this type of ice sublimation likely occurs also in NGC 253 with frequent shocks (Meier et al. 2015). The locations with enhanced HOCO<sup>+</sup> abundances are considered as intersections of different orbits. As shown in Figure 1, bar orbits ( $x_1$  orbits) and inner orbits ( $x_2$  orbits) intersect at the northeast and southwest parts of the CMZ, near GMCs 1, 8, 9, and 10. Shocks at GMCs 1, 2, 7, 8, 9, and 10 have been suggested by the detection of Class I methanol masers (Humire et al. 2022), and some other molecular tracers of shocks (Huang et al. in preparation). Because these regions are located at intersections of different orbits (bar and nuclear ring; see Sorai et al. 2000; Das et al. 2001; Levy et al. 2022, for the dynamical modeling), shocks due to cloud collisions are not surprising.

If the shock scenario is correct, ice sputtering of other species in addition to CO<sub>2</sub> should be taking place. Methanol enhancement shown in Section 3 is one example supporting this scenario. Water is another species abundant in ice, and ice sputtering should increase its gas-phase abundance. From the H<sub>2</sub>O/CO<sub>2</sub> ratio of  $\sim 7$  in ice (Yamagishi et al. 2015) and our estimated gas-

phase fractional abundance of CO<sub>2</sub> of  $(1 - 20) \times 10^{-7}$ , the gas-phase water abundances in shocked regions must be  $\sim (0.7 - 14) \times 10^{-6}$ . This estimate assumes that the same fraction of CO<sub>2</sub> and H<sub>2</sub>O ice is sublimated, and does not consider the higher desorption energy of water compared with CO<sub>2</sub>. It also assumes that gas-phase reactions subsequent to sputtering do not change the CO<sub>2</sub>/H<sub>2</sub>O ratio. Liu et al. (2017) derived fractional abundances of gas-phase water to be  $\sim 10^{-7}$  from Herschel HIFI/PACS/SPIRE data using multiple transitions of water in analysis with all data convolved to 40'' at the center of NGC 253. This value may be locally higher in shocked regions. However, it is impossible to confirm it without spatially resolving shocked regions and nuclear starburst regions with a higher-angular-resolution ( $< 10''$ ) observation.

Another possible CO<sub>2</sub> sublimation mechanism is thermal desorption. We do not know the distribution of the dust temperature due to the lack of high angular resolution data at the wavelengths of the peak black body radiation intensity ( $\sim 10 - 100 \mu\text{m}$  for 30-300 K). Yet, we do know that the most active star formation takes place around GMCs 3-5 from radio recombination line or 3mm continuum data (Bendo et al. 2015; Harada et al. 2021). If the hot/warm dust components are concentrated in GMCs 3-5, it is unlikely that the thermal desorption already takes place at GMCs 1 and 9. Therefore, thermal desorption unlikely contributes to the sublimation of CO<sub>2</sub> in GMCs 1, 2, 8, and 9. However, it is quite possible that thermal desorption occurs around GMC 3-5 due to the high dust temperature.

Another mechanism which can sublimate CO<sub>2</sub> is cosmic-ray-induced desorption as described in Section 6.3. We argued that this desorption mechanism is unlikely unless the dust is warm so that the maximum dust temperature achieved from cosmic-ray heating of dust becomes significantly larger than 70 K. Without high star formation rates in GMCs 1 and 9, it is unlikely that the dust is already warm.

For the reasons above, we conclude that a shock is the most likely scenario driving the CO<sub>2</sub> evaporation. Yet, to better constrain the ice fractional abundances, high angular resolution observations at infrared wavelengths, e.g., from JWST, are crucial.

## 7. SUMMARY

In this paper, we analyzed the abundances of HOCO<sup>+</sup>, the protonated form of CO<sub>2</sub>, in the central molecular zone of the starburst galaxy NGC 253, and discussed its relationship with the gas-and ice-phase CO<sub>2</sub>. Below is the summary of our findings.

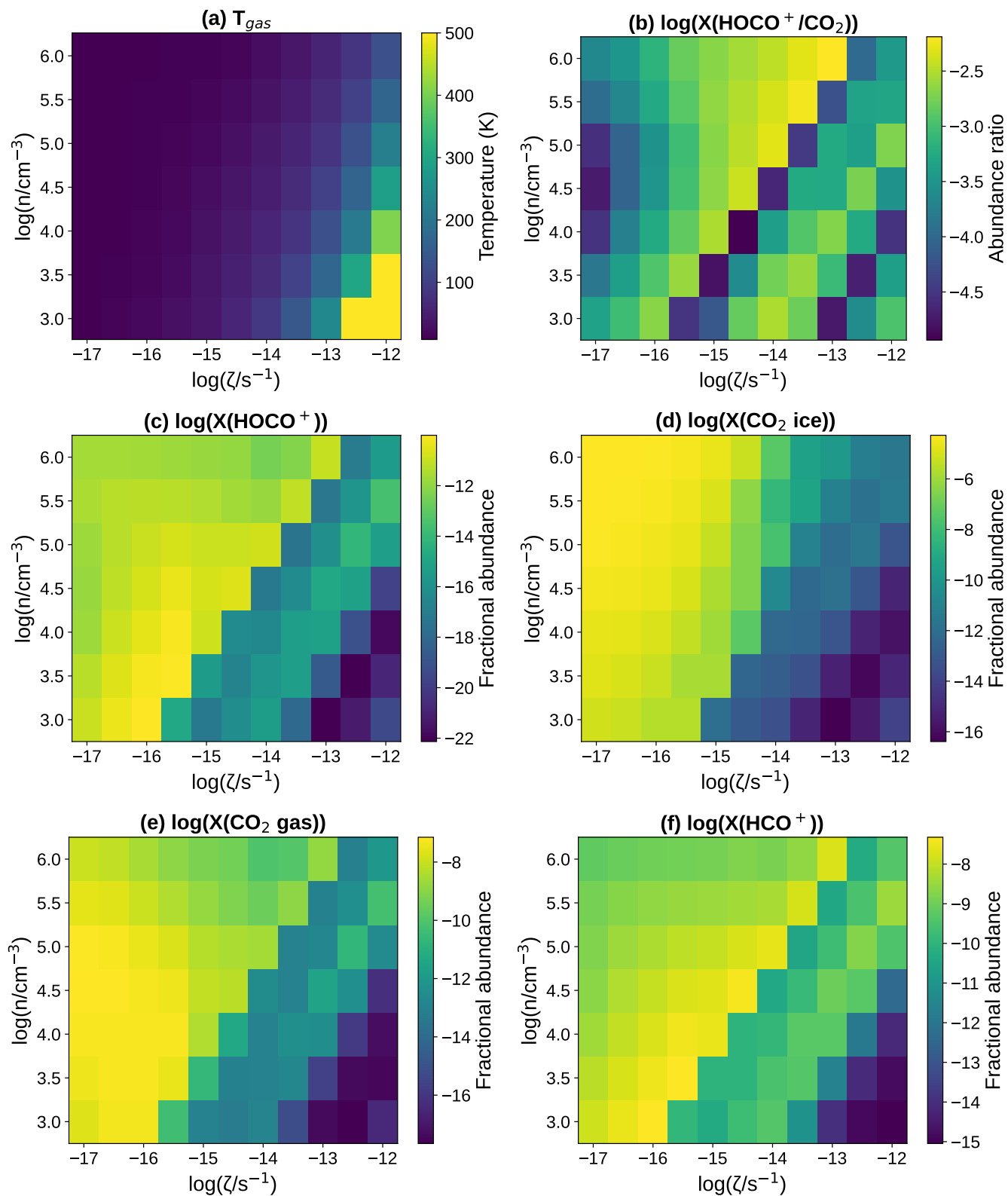


**Figure 6.** Following modeled quantities are shown as functions of the density and cosmic-ray ionization rate: (a) gas temperatures from the Meudon code used for Nautilus chemical modeling (b) abundance ratios  $\text{HOCO}^+/\text{CO}_2$  (c) fractional abundances of  $\text{HOCO}^+$ , (d)  $\text{CO}_2$  ice (surface + mantle), (e)  $\text{CO}_2$  gas, and (f)  $\text{HCO}^+$

- The distribution of HOCO<sup>+</sup> shows clear enhancements at locations of  $x_1$  and  $x_2$  orbital intersections where shocks are expected. This distribution is similar to that of methanol but is different from that of H<sup>13</sup>CO<sup>+</sup>. There are two formation routes of HOCO<sup>+</sup>; one is the ion-neutral reaction HCO<sup>+</sup> + OH and the other is the protonation of CO<sub>2</sub>. If the former route is dominant, the HOCO<sup>+</sup> distribution should be similar to that of HCO<sup>+</sup>, while the latter route should cause similarity with the CH<sub>3</sub>OH distribution. Therefore, HOCO<sup>+</sup> is likely produced through the protonation of CO<sub>2</sub>.
- We derive HOCO<sup>+</sup> column densities across the CMZ using CASSIS, from which we also obtain its fractional abundances using the total H<sub>2</sub> column densities estimated from the dust emission. We find HOCO<sup>+</sup> fractional abundances as high as  $\sim 2 \times 10^{-9}$ , which is similar to those observed in the Galactic center, but orders of magnitude higher than those reported in Galactic spiral-arm molecular clouds.
- From the results of chemical modeling and values of cosmic-ray ionization rates derived from previous ALCHEMI works, we estimate that the gaseous HOCO<sup>+</sup>/CO<sub>2</sub> ratio is likely  $10^{-3} - 10^{-2}$ . This ratio suggests that the gas-phase CO<sub>2</sub> fractional abundances are  $(1 - 20) \times 10^{-7}$  at peaks of HOCO<sup>+</sup> emission.
- We also estimate fractional abundances of CO<sub>2</sub> ice from their column densities in the literature. The ice fractional abundance at the HOCO<sup>+</sup> peak is similar to the value in the Galactic interstellar medium ( $10^{-6} - 10^{-5}$ ), but is lower ( $\sim (1 - 3) \times 10^{-7}$ ) near the NGC 253 galactic center.
- The increased gaseous and ice fractional abundances of CO<sub>2</sub> at the outer CMZ of NGC 253 imply that a large fraction of ice is sublimated. Because of the association of these locations with evidence of shocks, we propose that this efficient sublimation is attributed to shock-induced sputtering.

High spatial resolution observations of molecular emission in external galaxies, such as those performed by the ALCHEMI survey toward the central regions of the starburst galaxy NGC 253 with ALMA, have greatly improved our understanding of gas-phase abundances and will continue to do so. Now, complementary observations of ice at high angular resolutions with the JWST

are required to obtain a complete picture of the chemical processes in starburst galaxies.

1 We thank the anonymous referee for constructive  
 2 comments. N.H. thanks Hideko Nomura for the  
 3 helpful discussion on CO<sub>2</sub> transitions in the infrared  
 4 wavelength, and Kotomi Taniguchi for the initial help  
 5 using CASSIS. This paper makes use of the following  
 6 ALMA data: ADS/JAO.ALMA#2017.1.00161.L,  
 7 ADS/JAO.ALMA#2018.1.00162.S,  
 8 ADS/JAO.ALMA#2018.1.01321.S. ALMA is a part-  
 9 nership of ESO (representing its member states),  
 10 NSF (USA) and NINS (Japan), together with NRC  
 11 (Canada), MOST and ASIAA (Taiwan), and KASI  
 12 (Republic of Korea), in cooperation with the Republic  
 13 of Chile. The National Radio Astronomy Observatory  
 14 is a facility of the National Science Foundation operated  
 15 under cooperative agreement by Associated Universi-  
 16 ties, Inc. The Joint ALMA Observatory is operated by  
 17 ESO, AUI/NRAO and NAOJ. Data analysis was in part  
 18 carried out on the Multi-wavelength Data Analysis Sys-  
 19 tem operated by the Astronomy Data Center (ADC),  
 20 National Astronomical Observatory of Japan. N.H.  
 21 acknowledges support from JSPS KAKENHI Grant  
 22 Number JP21K03634. V.M.R. has received support  
 23 from the Comunidad de Madrid through the Atracción  
 24 de Talento Investigador Modalidad 1 (Doctores con  
 25 experiencia) Grant (COOL:Cosmic Origins of Life;  
 26 2019-T1/TIC-5379), and the Ayuda RYC2020-029387-I  
 27 funded by MCIN/AEI /10.13039/501100011033. L.C.  
 28 has received partial support from the Spanish State  
 29 Research Agency (AEI; project number PID2019-  
 30 105552RB-C41). P.H. is a member of and received  
 31 financial support for this research from the Inter-  
 32 national Max Planck Research School (IMPRS) for  
 33 Astronomy and Astrophysics at the Universities of  
 34 Bonn and Cologne. K.S. is supported by the grant  
 35 MOST 109-2112-M-001-020 from the Ministry of Sci-  
 36 ence and Technology, Taiwan. This research has made  
 37 use of the NASA/IPAC Extragalactic Database (NED),  
 38 which is funded by the National Aeronautics and Space  
 39 Administration and operated by the California Institute  
 40 of Technology.

*Facilities:* ALMA

*Software:* Astropy (Astropy Collaboration et al. 2013, 2018), CASA (McMullin et al. 2007), CASSIS (Vas-  
 41 tel et al. 2015), Nautilus (Rauud et al. 2016)

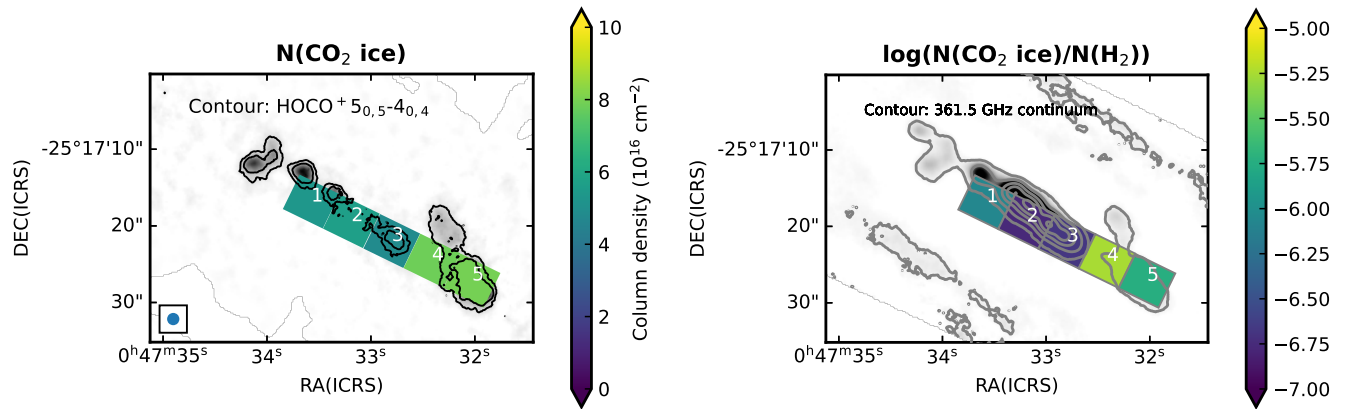


**Figure 7.** (Left) Column densities of CO<sub>2</sub> ice reported by Yamagishi et al. (2015) are shown for selected slits in color. The integrated intensity image of HOCO<sup>+</sup> (5<sub>0,5</sub>-4<sub>0,4</sub>) is shown both in contours and grey scale. (Right) Fractional abundances of CO<sub>2</sub> ice (i.e., CO<sub>2</sub> ice column densities divided by the averaged total H<sub>2</sub> column densities inside rectangular regions) are shown in log scale with colored rectangles. The continuum image at 361.5 GHz is shown in contours and grey scale.



## A. CASSIS FITTING PARAMETERS

CASSIS constrains parameters such as column density, line velocity, line width (full width at half maximum; FWHM), excitation temperatures, and source sizes by fitting the spectra. We used the MCMC algorithm provided by CASSIS to derive these parameters. We use spectra from transitions shown in the upper half of Table 1. When using the MCMC method, users provide acceptable ranges of these parameters as well as the initial guesses. We used the column density range of  $[10^{12}, 10^{16}] \text{ cm}^{-2}$  with the initial guess of  $10^{14} \text{ cm}^{-2}$ , the excitation temperature range  $[5, 50] \text{ K}$  with the initial guess of  $6 \text{ K}$ , the velocity range  $[v_{\text{CO}} - 30, v_{\text{CO}} + 30.] \text{ km s}^{-1}$  where  $v_{\text{CO}}$  is the velocity obtained from the moment 1 image of CO(1-0), which is also used for the initial guess. The range of FWHM we used is  $[\sigma_V - 20., 90.] \text{ km s}^{-1}$  with the initial guess of  $\sigma_V$  where  $\sigma_V$  is the velocity dispersion of the CO(1-0) image<sup>6</sup>. We note that the line width of HOCO<sup>+</sup> is significantly different from that of CO(1-0), and this range of FWHM is simply determined by running CASSIS multiple times and checking the range to produce a reasonable fit.

Uncertainties from the CASSIS fit are reasonably small for most cases. Figure 8(left) shows that the errors of the column densities are around 10% for most cases, and  $\sim 20 - 30\%$  for a small fraction of pixels with low signal-to-noise ratios. Uncertainties in excitation temperatures are within 0.5 K for most pixels, with a maximum of 3 K.

There are also other sources of uncertainties, in addition to the spectral fitting. For example, HOCO<sup>+</sup> column densities derived with spectroscopic constants from Jet Propulsion Laboratory (JPL; <https://spec.jpl.nasa.gov/>) would yield up to a factor of 2 larger values compared with ones from CDMS. Although this is a large factor, a use of different spectroscopic constants changes the results uniformly within the field of view. There are also observational uncertainties of up to 15% (Martín et al. 2021). These uncertainties will not change our main conclusions.

The HOCO<sup>+</sup> transitions are optically thin even where the column densities are high. CASSIS does not provide the optical depths, but we also ran MADCUBA (Martín et al. 2019), a similar spectral fitting software to obtain optical depths. The optical depths are  $< 0.1$  for positions that we checked, which have high intensities of HOCO<sup>+</sup>.

The modeled intensities with CASSIS for pixels that are closest to each GMC position are shown in Table 2 if HOCO<sup>+</sup> transition for a GMC is detected.

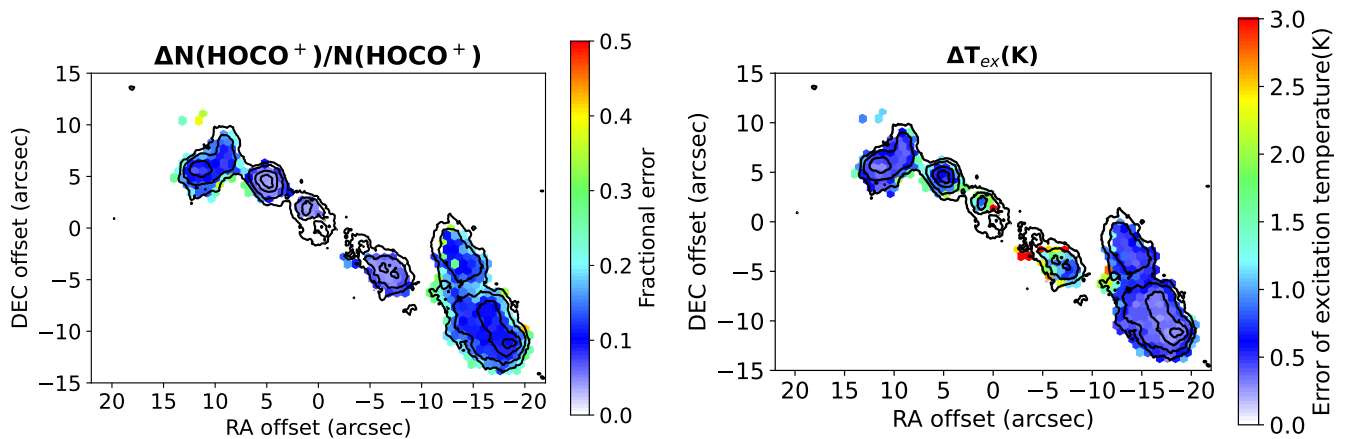


**Figure 8.** (Left) Ratios of errors in the derivation of HOCO<sup>+</sup> column densities over the derived HOCO<sup>+</sup> column densities at corresponding hexagonal pixels. (Right) Errors of excitation temperatures.

## B. ICE DATA FROM AKARI

Here we summarize analyses by Yamagishi et al. (2015), and present spectra for regions used in our analysis. The observed wavelength range is about  $2.5 - 5.0 \mu\text{m}$ . Within this range, CO<sub>2</sub> ice, H<sub>2</sub>O ice, Br $\alpha$ , and PAH  $3.3 \mu\text{m}$  features were detected in addition to the continuum. CO<sub>2</sub> ice features at  $4.27 \mu\text{m}$  are fit using the data range of  $4.1 - 4.4 \mu\text{m}$  as there is only this narrow ice feature in this wavelength range. Because the ice com-

<sup>6</sup> The relationship between the FWHM and the standard deviation of a Gaussian distribution is usually described as  $FWHM \sim 2.355\sigma_V$ . In our case, the line width of HOCO<sup>+</sup> is much smaller than that of CO(1-0), and the initial guess of  $\sigma_V$  for the FWHM of HOCO<sup>+</sup> is still a reasonable one.

**Table 2.** Modeled integrated intensities

GMC	$x_{\text{offset}}$	$y_{\text{offset}}$	$\int I dv$					
	( $''$ )	( $''$ )	( $4_{0,4} - 3_{0,3}$ )	( $5_{0,5} - 4_{0,4}$ )	( $6_{0,6} - 5_{0,5}$ )	( $7_{0,7} - 6_{0,6}$ )	( $8_{0,8} - 7_{0,7}$ )	( $12_{0,12} - 11_{0,11}$ )
1	-17.3,	-10.4	12.14	9.00	5.25	2.47	0.94	0.00
2	-13.6,	-2.8	6.40	4.93	2.92	1.39	0.55	0.00
3	-6.5,	-4.2	6.39	7.99	8.96	9.06	8.36	3.02
6	0.4,	2.1	4.41	6.05	7.42	8.37	8.81	6.28
7	4.8,	4.2	11.12	12.40	11.84	9.95	7.48	0.88
8	10.0,	6.2	7.30	6.05	4.03	2.22	1.01	0.01
9	12.0,	5.6	13.08	10.73	7.11	3.85	1.73	0.01

NOTE—Integrated intensities of HOCO<sup>+</sup> transitions produced by CASSIS fitting for hexagonal pixels closest to GMCs. Results are shown only for GMCs with HOCO<sup>+</sup> detection.

position changes the spectral shape, multiple ice compositions were tested to best fit the spectra. Consequently, the ice composition of H<sub>2</sub>O:CH<sub>3</sub>OH:CO<sub>2</sub>=9 : 1 : 2 was used in the final analysis.

Figure 9 shows spectra used to derive CO<sub>2</sub> ice column densities shown in Figure 7. Note that our Regions 1-5 correspond to ID 47-51 in Table 3 of Yamagishi et al. (2015).

### C. GMC POSITIONS

As already noted in Humire et al. (2022) and Behrens et al. (submitted to ApJ), the GMC nomenclature was adopted from Leroy et al. (2015), but with modified positions. How these modifications are made is explained

in Behrens et al. (submitted to ApJ). These positions are shown in Table 3.

### D. THE ARCHIVAL CO(2-1) IMAGE

The large-scale CO(2-1) image of NGC 253 shown in Figure 1 was taken from the ALMA archive (project code #2018.1.01321.S). These data use the configuration consisting on the 7-m array complemented by the total power antenna. Pipeline-reduced image cubes (QA2 products) for the 7-m array and total power single-dish data were combined with the CASA command `feather`. This image was shown to indicate the rough positions of  $x_1$  and  $x_2$  orbits only. We expect that the PI team will present the data with better imaging quality and scientific analysis.

### REFERENCES

- Agúndez, M., Cernicharo, J., de Vicente, P., et al. 2015, *A&A*, 579, L10, doi: [10.1051/0004-6361/201526650](https://doi.org/10.1051/0004-6361/201526650)
- Aladro, R., Martín, S., Riquelme, D., et al. 2015, *A&A*, 579, A101, doi: [10.1051/0004-6361/201424918](https://doi.org/10.1051/0004-6361/201424918)
- Armijos-Abendaño, J., Martín-Pintado, J., Requena-Torres, M. A., Martín, S., & Rodríguez-Franco, A. 2015, *MNRAS*, 446, 3842, doi: [10.1093/mnras/stu2271](https://doi.org/10.1093/mnras/stu2271)
- Astropy Collaboration, Robitaille, T. P., Tollerud, E. J., et al. 2013, *A&A*, 558, A33, doi: [10.1051/0004-6361/201322068](https://doi.org/10.1051/0004-6361/201322068)
- Astropy Collaboration, Price-Whelan, A. M., Sipőcz, B. M., et al. 2018, *AJ*, 156, 123, doi: [10.3847/1538-3881/aabc4f](https://doi.org/10.3847/1538-3881/aabc4f)
- Athanassoula, E. 1992, *MNRAS*, 259, 345, doi: [10.1093/mnras/259.2.345](https://doi.org/10.1093/mnras/259.2.345)
- Bendo, G. J., Beswick, R. J., D’Cruze, M. J., et al. 2015, *MNRAS*, 450, L80, doi: [10.1093/mnrasl/slv053](https://doi.org/10.1093/mnrasl/slv053)
- Bizzocchi, L., Lattanzi, V., Laas, J., et al. 2017, *A&A*, 602, A34, doi: [10.1051/0004-6361/201730638](https://doi.org/10.1051/0004-6361/201730638)
- Bolatto, A. D., Warren, S. R., Leroy, A. K., et al. 2013, *Nature*, 499, 450, doi: [10.1038/nature12351](https://doi.org/10.1038/nature12351)
- Boonman, A. M. S., van Dishoeck, E. F., Lahuis, F., & Doty, S. D. 2003, *A&A*, 399, 1063, doi: [10.1051/0004-6361:20021868](https://doi.org/10.1051/0004-6361:20021868)
- Cohen, D. P., Turner, J. L., & Consiglio, S. M. 2020, *MNRAS*, 493, 627, doi: [10.1093/mnras/staa292](https://doi.org/10.1093/mnras/staa292)

**Table 3.** GMC positions

ID	RA (ICRS)	DEC (ICRS)
	00 <sup>h</sup> 47 <sup>m</sup> – <sup>s</sup>	–25°17′–″
1	32.02	28.2
2	32.28	20.2
3	32.81	21.6
4	32.97	20.0
5	33.21	17.4
6	33.33	15.8
7	33.64	13.3
8	34.02	11.4
9	34.17	12.3
10	34.24	7.8

NOTE—Modified coordinates of GMC positions in Leroy et al. (2015) provided by A. K. Leroy (private communication).

- Dale, D. A., Cohen, S. A., Johnson, L. C., et al. 2009, *ApJ*, 703, 517, doi: [10.1088/0004-637X/703/1/517](https://doi.org/10.1088/0004-637X/703/1/517)
- Das, M., Anantharamaiah, K. R., & Yun, M. S. 2001, *ApJ*, 549, 896, doi: [10.1086/319430](https://doi.org/10.1086/319430)
- Defrees, D. J., Loew, G. H., & McLean, A. D. 1982, *ApJ*, 254, 405, doi: [10.1086/159745](https://doi.org/10.1086/159745)
- Flower, D. R., & Pineau des Forêts, G. 2012, *MNRAS*, 421, 2786, doi: [10.1111/j.1365-2966.2012.20481.x](https://doi.org/10.1111/j.1365-2966.2012.20481.x)
- Fontani, F., Vagnoli, A., Padovani, M., et al. 2018, *Monthly Notices of the Royal Astronomical Society*, 481, 79, doi: [10.1093/mnras/sly160](https://doi.org/10.1093/mnras/sly160)
- García-Burillo, S., Martín-Pintado, J., Fuente, A., & Neri, R. 2000, *A&A*, 355, 499, <https://arxiv.org/abs/astro-ph/0001173>
- Garrod, R. T., & Pauly, T. 2011, *ApJ*, 735, 15, doi: [10.1088/0004-637X/735/1/15](https://doi.org/10.1088/0004-637X/735/1/15)
- Garrod, R. T., Wakelam, V., & Herbst, E. 2007, *A&A*, 467, 1103, doi: [10.1051/0004-6361:20066704](https://doi.org/10.1051/0004-6361:20066704)
- Haasler, D., Rivilla, V. M., Martín, S., et al. 2022, *A&A*, 659, A158, doi: [10.1051/0004-6361/202142032](https://doi.org/10.1051/0004-6361/202142032)
- Harada, N., Sakamoto, K., Martín, S., et al. 2019, *ApJ*, 884, 100, doi: [10.3847/1538-4357/ab41ff](https://doi.org/10.3847/1538-4357/ab41ff)
- Harada, N., Riquelme, D., Viti, S., et al. 2015, *A&A*, 584, A102, doi: [10.1051/0004-6361/201526994](https://doi.org/10.1051/0004-6361/201526994)
- Harada, N., Martín, S., Mangum, J. G., et al. 2021, *ApJ*, 923, 24, doi: [10.3847/1538-4357/ac26b8](https://doi.org/10.3847/1538-4357/ac26b8)
- Hasegawa, T. I., & Herbst, E. 1993, *MNRAS*, 261, 83, doi: [10.1093/mnras/261.1.83](https://doi.org/10.1093/mnras/261.1.83)
- Herbst, E., Green, S., Thaddeus, P., & Klemperer, W. 1977, *ApJ*, 215, 503, doi: [10.1086/155381](https://doi.org/10.1086/155381)
- Hildebrand, R. H. 1983, *QJRAS*, 24, 267
- Holdship, J., Viti, S., Martín, S., et al. 2021, *A&A*, 654, A55, doi: [10.1051/0004-6361/202141233](https://doi.org/10.1051/0004-6361/202141233)
- Holdship, J., Mangum, J. G., Viti, S., et al. 2022, *arXiv e-prints*, arXiv:2204.03668, <https://arxiv.org/abs/2204.03668>
- Humire, P. K., Henkel, C., Hernández-Gómez, A., et al. 2022, *arXiv e-prints*, arXiv:2205.03281, <https://arxiv.org/abs/2205.03281>
- Jiménez-Serra, I., Caselli, P., Martín-Pintado, J., & Hartquist, T. W. 2008, *A&A*, 482, 549, doi: [10.1051/0004-6361:20078054](https://doi.org/10.1051/0004-6361:20078054)
- Kalvāns, J., & Kalnin, J. R. 2020, *A&A*, 633, A97, doi: [10.1051/0004-6361/201936471](https://doi.org/10.1051/0004-6361/201936471)
- Kim, W.-T., Seo, W.-Y., & Kim, Y. 2012, *ApJ*, 758, 14, doi: [10.1088/0004-637X/758/1/14](https://doi.org/10.1088/0004-637X/758/1/14)
- Krieger, N., Bolatto, A. D., Walter, F., et al. 2019, *The Astrophysical Journal*, 881, 43, doi: [10.3847/1538-4357/ab2d9c](https://doi.org/10.3847/1538-4357/ab2d9c)
- Lahuis, F., Spoon, H. W. W., Tielens, A. G. G. M., et al. 2007, *ApJ*, 659, 296, doi: [10.1086/512050](https://doi.org/10.1086/512050)
- Le Petit, F., Nehmé, C., Le Bourlot, J., & Roueff, E. 2006, *ApJS*, 164, 506, doi: [10.1086/503252](https://doi.org/10.1086/503252)
- Leroy, A. K., Bolatto, A. D., Ostriker, E. C., et al. 2015, *The Astrophysical Journal*, 801, doi: [10.1088/0004-637X/801/1/25](https://doi.org/10.1088/0004-637X/801/1/25)

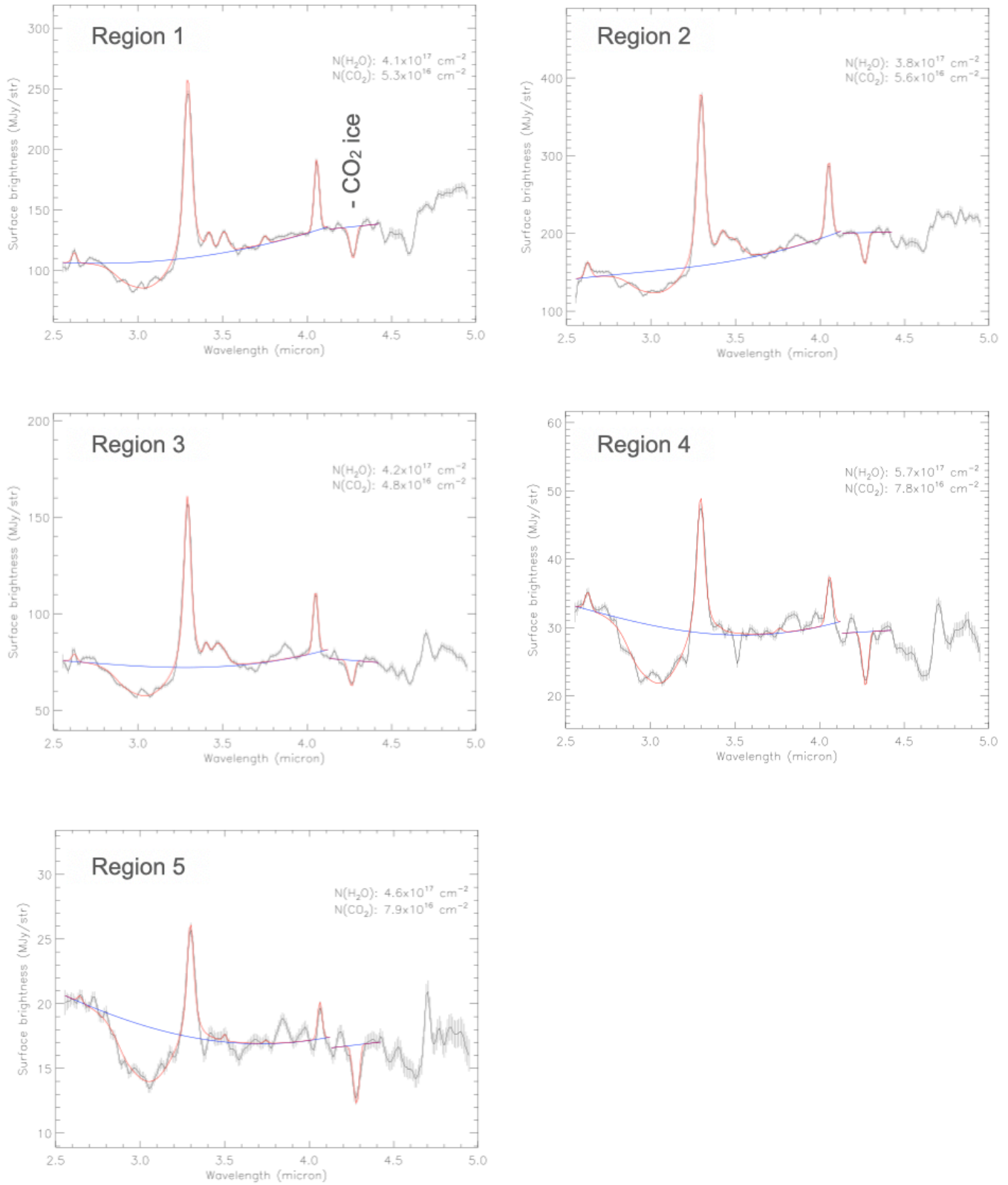


**Figure 9.** AKARI spectra for regions used in our analysis. As in Figure 1 of Yamagishi et al. (2015), the blue curve represents the best-fit continuum emission while the red curve shows the overall spectral profiles.

- Levy, R. C., Bolatto, A. D., Leroy, A. K., et al. 2022, arXiv e-prints, arXiv:2206.04700.  
<https://arxiv.org/abs/2206.04700>
- Liu, L., Weiß, A., Perez-Beaupuits, J. P., et al. 2017, *ApJ*, 846, 5, doi: [10.3847/1538-4357/aa81b4](https://doi.org/10.3847/1538-4357/aa81b4)
- LVL team. 2009, Spitzer Local Volume Legacy Survey, IPAC, doi: [10.26131/IRSA414](https://doi.org/10.26131/IRSA414)
- Majumdar, L., Gratier, P., Wakelam, V., et al. 2018, *Monthly Notices of the Royal Astronomical Society*, 477, 525, doi: [10.1093/mnras/sty703](https://doi.org/10.1093/mnras/sty703)
- Mangum, J. G., Ginsburg, A. G., Henkel, C., et al. 2019, *The Astrophysical Journal*, 871, 170, doi: [10.3847/1538-4357/aafa15](https://doi.org/10.3847/1538-4357/aafa15)
- Martín, S., Martín-Pintado, J., Blanco-Sánchez, C., et al. 2019, *A&A*, 631, A159, doi: [10.1051/0004-6361/201936144](https://doi.org/10.1051/0004-6361/201936144)
- Martín, S., Mauersberger, R., Martín-Pintado, J., Henkel, C., & García-Burillo, S. 2006, *ApJS*, 164, 450, doi: [10.1086/503297](https://doi.org/10.1086/503297)
- Martín, S., Mangum, J. G., Harada, N., et al. 2021, *A&A*, 656, A46, doi: [10.1051/0004-6361/202141567](https://doi.org/10.1051/0004-6361/202141567)
- McMullin, J. P., Waters, B., Schiebel, D., Young, W., & Golap, K. 2007, in *Astronomical Society of the Pacific Conference Series*, Vol. 376, *Astronomical Data Analysis Software and Systems XVI*, ed. R. A. Shaw, F. Hill, & D. J. Bell, 127
- Meier, D. S., & Turner, J. L. 2005, *ApJ*, 618, 259, doi: [10.1086/426499](https://doi.org/10.1086/426499)
- Meier, D. S., Walter, F., Bolatto, A. D., et al. 2015, *ApJ*, 801, 63, doi: [10.1088/0004-637X/801/1/63](https://doi.org/10.1088/0004-637X/801/1/63)
- Menten, K. M., Wilson, R. W., Leurini, S., & Schilke, P. 2009, *ApJ*, 692, 47, doi: [10.1088/0004-637X/692/1/47](https://doi.org/10.1088/0004-637X/692/1/47)
- Minh, Y. C., Brewer, M. K., Irvine, W. M., Friberg, P., & Johansson, L. E. B. 1991, *Astronomy and Astrophysics*, Vol. 244, p. 470 (1991), 244, 470. <https://ui.adsabs.harvard.edu/abs/1991A%26A...244..470M/abstract>
- Minh, Y. C., Irvine, W. M., & Ziurys, L. M. 1988, *The Astrophysical Journal*, 334, 175, doi: [10.1086/166827](https://doi.org/10.1086/166827)
- Minissale, M., Congiu, E., Manicò, G., Pironello, V., & Dulieu, F. 2013, *A&A*, 559, A49, doi: [10.1051/0004-6361/201321453](https://doi.org/10.1051/0004-6361/201321453)
- Minissale, M., Loison, J. C., Baouche, S., et al. 2015, *A&A*, 577, A2, doi: [10.1051/0004-6361/201424342](https://doi.org/10.1051/0004-6361/201424342)
- Minissale, M., Aikawa, Y., Bergin, E., et al. 2022, arXiv e-prints, arXiv:2201.07512.  
<https://arxiv.org/abs/2201.07512>
- Müller, H. S. P., Schlöder, F., Stutzki, J., & Winnewisser, G. 2005, *Journal of Molecular Structure*, 742, 215, doi: [10.1016/j.molstruc.2005.01.027](https://doi.org/10.1016/j.molstruc.2005.01.027)
- Müller, H. S. P., Thorwirth, S., Roth, D. A., & Winnewisser, G. 2001, *A&A*, 370, L49, doi: [10.1051/0004-6361:20010367](https://doi.org/10.1051/0004-6361:20010367)
- Muller, S., Beelen, A., Black, J. H., et al. 2013, *A&A*, 551, A109, doi: [10.1051/0004-6361/201220613](https://doi.org/10.1051/0004-6361/201220613)
- Müller-Sánchez, F., González-Martín, O., Fernández-Ontiveros, J. A., Acosta-Pulido, J. A., & Prieto, M. A. 2010, *ApJ*, 716, 1166, doi: [10.1088/0004-637X/716/2/1166](https://doi.org/10.1088/0004-637X/716/2/1166)
- Öberg, K. I., Boogert, A. C. A., Pontoppidan, K. M., et al. 2011, *ApJ*, 740, 109, doi: [10.1088/0004-637X/740/2/109](https://doi.org/10.1088/0004-637X/740/2/109)
- Öberg, K. I., Linnartz, H., Visser, R., & van Dishoeck, E. F. 2009a, *ApJ*, 693, 1209, doi: [10.1088/0004-637X/693/2/1209](https://doi.org/10.1088/0004-637X/693/2/1209)
- Öberg, K. I., van Dishoeck, E. F., & Linnartz, H. 2009b, *A&A*, 496, 281, doi: [10.1051/0004-6361/200810207](https://doi.org/10.1051/0004-6361/200810207)
- Pérez-Beaupuits, J. P., Güsten, R., Harris, A., et al. 2018, *ApJ*, 860, 23, doi: [10.3847/1538-4357/aabe8e](https://doi.org/10.3847/1538-4357/aabe8e)
- Rekola, R., Richer, M. G., McCall, M. L., et al. 2005, *MNRAS*, 361, 330, doi: [10.1111/j.1365-2966.2005.09166.x](https://doi.org/10.1111/j.1365-2966.2005.09166.x)
- Rico-Villas, F., Martín-Pintado, J., González-Alfonso, E., Martín, S., & Rivilla, V. M. 2020, *MNRAS*, 491, 4573, doi: [10.1093/mnras/stz3347](https://doi.org/10.1093/mnras/stz3347)
- Rivilla, V. M., Martín-Pintado, J., Jiménez-Serra, I., et al. 2019, *MNRAS*, 483, L114, doi: [10.1093/mnrasl/sly228](https://doi.org/10.1093/mnrasl/sly228)
- Ruaud, M., Wakelam, V., & Hersant, F. 2016, *MNRAS*, 459, 3756, doi: [10.1093/mnras/stw887](https://doi.org/10.1093/mnras/stw887)
- Sakai, N., Sakai, T., Aikawa, Y., & Yamamoto, S. 2008, *The Astrophysical Journal*, 675, L89, doi: [10.1086/533463](https://doi.org/10.1086/533463)
- Sakamoto, K., Mao, R.-Q., Matsushita, S., et al. 2011, *The Astrophysical Journal*, 735, doi: [10.1088/0004-637X/735/1/19](https://doi.org/10.1088/0004-637X/735/1/19)
- Sakamoto, K., Ho, P. T. P., Iono, D., et al. 2006, *The Astrophysical Journal*, 636, 685, doi: [10.1086/498075](https://doi.org/10.1086/498075)
- Seo, W.-Y., & Kim, W.-T. 2013, *ApJ*, 769, 100, doi: [10.1088/0004-637X/769/2/100](https://doi.org/10.1088/0004-637X/769/2/100)
- Sorai, K., Nakai, N., Kuno, N., Nishiyama, K., & Hasegawa, T. 2000, *PASJ*, 52, 785, doi: [10.1093/pasj/52.5.785](https://doi.org/10.1093/pasj/52.5.785)
- Sormani, M. C., & Li, Z. 2020, *MNRAS*, 494, 6030, doi: [10.1093/mnras/staa1139](https://doi.org/10.1093/mnras/staa1139)
- Thaddeus, P., Guelin, M., & Linke, R. A. 1981, *ApJL*, 246, L41, doi: [10.1086/183549](https://doi.org/10.1086/183549)
- Turner, B. E., Terzieva, R., & Herbst, E. 1999, *The Astrophysical Journal*, 518, 699, doi: [10.1086/307300](https://doi.org/10.1086/307300)
- Turner, J. L., & Ho, P. T. P. 1985, *The Astrophysical Journal*, 299, L77, doi: [10.1086/184584](https://doi.org/10.1086/184584)
- Vastel, C., Bottinelli, S., Caux, E., Glorian, J. M., & Boiziot, M. 2015, in *SF2A-2015: Proceedings of the Annual meeting of the French Society of Astronomy and Astrophysics*, 313–316

Vastel, C., Ceccarelli, C., Lefloch, B., & Bachiller, R. 2016, *A&A*, 591, L2, doi: [10.1051/0004-6361/201628427](https://doi.org/10.1051/0004-6361/201628427)

Viti, S., Jimenez-Serra, I., Yates, J. A., et al. 2011, *ApJL*, 740, L3, doi: [10.1088/2041-8205/740/1/L3](https://doi.org/10.1088/2041-8205/740/1/L3)

Wakelam, V., Loison, J. C., Mereau, R., & Ruaud, M. 2017, *Molecular Astrophysics*, 6, 22, doi: [10.1016/j.molap.2017.01.002](https://doi.org/10.1016/j.molap.2017.01.002)

Yamagishi, M., Kaneda, H., Ishihara, D., et al. 2015, *ApJ*, 807, 29, doi: [10.1088/0004-637X/807/1/29](https://doi.org/10.1088/0004-637X/807/1/29)